Quaternary Science Reviews 163 (2017) 95–113

Contents lists available at ScienceDirect

Quaternary Science Reviews

journal homepage: www.elsevier.com/locate/quascirev

North-African paleodrainage discharges to the central Mediterranean during the last 18,000 years: A multiproxy characterization

Jiawang Wu [a, *], Zhifei Liu [b], Jan-Berend W. Stuut [c, d], Yulong Zhao [b], Antonio Schirone [e], Gert J. de Lange [a]

[a] Department of Earth Sciences – Geochemistry, Utrecht University, 3584 CC Utrecht, The Netherlands
[b] State Key Laboratory of Marine Geology, Tongji University, 200092 Shanghai, China
[c] NIOZ, Royal Netherlands Institute for Sea Research, Utrecht University, 1790 AB Den Burg, The Netherlands
[d] MARUM, Center for Marine Environmental Sciences, Bremen University, 28359 Bremen, Germany
[e] ENEA, Marine Environment Research Centre, P.O. Box 224, 19100 La Spezia, Italy

ARTICLE INFO

Article history:
Received 2 January 2017
Received in revised form
13 March 2017
Accepted 16 March 2017
Available online 24 March 2017

Keywords:
Quaternary
Paleoclimatology
North Africa
Inorganic geochemistry
Clay minerals
Grain size end-member modeling
African humid period
Sapropel S1
Provenance
Paleodrainage systems

ABSTRACT

Using elemental geochemistry, clay mineralogy, grain size end-member modeling, and planktonic foraminiferal $\delta^{18}O$, we characterize the provenance of central-Mediterranean sediments over the past 18 ka. The provenance is dust-dominated before and after the African Humid Period (AHP). By contrast, during the AHP (~11–5 ka), largely concurrent with organic-rich sapropel S1 formation, it is predominantly riverine from North-African sources. Such fluvial supply is suggested to come from paleodrainage networks that were reactivated by intensified monsoon precipitation during the AHP. The supply is characterized by high Mg/Al and smectite contents, and has been accompanied by considerable freshwater influx, as indicated by the enhanced grain size and lighter foraminiferal $\delta^{18}O$. The clay-mineral assemblages in our core and in nearby cores correspond with a provenance from the Libyan-Tunisian margin, mainly via the paleo-river Irharhar. The inferred fluvial discharge is strongest during the late-AHP (~8–5.5 ka), coinciding with reported enhanced fluvial dynamics and wettest conditions over western Libya and Tunisia/Algeria. This period is not only synchronous with the largest extension of open-water bodies in North Africa and lowest Saharan dust inputs, but also consistent with precipitation records of the West-African monsoon. Moreover, our records show a remarkable correspondence with that of a paleodrainage system towards the Atlantic West-African margin, inferring a common headwater region in the central Saharan mountains, and a similar climate mechanism. Taken together, we suggest a dominant control of North-African humid surfaces on the paleodrainage delivery, modulated by groundwater level, in response to the insolation-driven West-African monsoon precipitation.

1. Introduction

In North Africa, a humid episode occurred between ~11 and 5 ka cal. BP (hereafter referred to as "ka"), which led to the development of a savannah-type vegetation cover and extensive fluvial networks over the presently hyperarid Saharan desert (e.g. Hoelzmann et al., 1998; Jolly et al., 1998; Drake et al., 2011; Lézine et al., 2011; Armitage et al., 2015). This so-called African Humid Period (AHP; c.f. deMenocal et al., 2000) not only had a major influence on the settlement of Neolithic communities (e.g. Kuper and Kröpelin, 2006; Drake et al., 2011; Manning and Timpson, 2014; Timmermann and Friedrich, 2016), but also resulted in enhanced fluvial discharge to the surrounding ocean margins, such as the equatorial Atlantic (Schefuß et al., 2005; Weldeab et al., 2007), western Sahara (Zühlsdorff et al., 2007; Tjallingii et al., 2008; Niedermeyer et al., 2010; Skonieczny et al., 2015), and north-eastern Africa (Almogi-Labin et al., 2009; Hennekam et al., 2014, 2015; Weldeab et al., 2014). Such enhanced freshwater influx to the eastern Mediterranean Sea (EMS) stimulated density stratification of the water column and was associated with higher productivity in the surface water. This ultimately caused deep-water stagnation and a basin-wide formation of the most-recent organic-rich unit, sapropel S1 (~10.8–6.1 ka) (Rohling, 1994; De Lange et al., 2008; Grimm et al., 2015; Filippidi et al., 2016). It is well understood that humid climatic conditions such as those during the AHP occurred repeatedly, in response to boreal precessional insolation

* Corresponding author.
E-mail address: j.w.wu@uu.nl (J. Wu).

http://dx.doi.org/10.1016/j.quascirev.2017.03.015
0277-3791/

maxima, associated with the strengthening of the African monsoon and the northward migration of the Intertropical Convergence Zone (ITCZ). This resulted in the rhythmic occurrence of sapropel units over the EMS (Rossignol-Strick et al., 1982; Tuenter et al., 2003; Zhao et al., 2012; Rohling et al., 2015).

Nevertheless, the exact mechanisms and sources for fluvial delivery and related changes are still insufficiently known. The monsoon-fed Nile discharge has been reported as the major freshwater source during sapropel formation (e.g. Rossignol-Strick et al., 1982; Freydier et al., 2001; Revel et al., 2010; Zhao et al., 2012; Hennekam et al., 2014). Increased precipitation and associated runoff from the Northern Borderlands of the Eastern Mediterranean (NBEM) may also constitute a considerable input (e.g. Kallel et al., 1997; Zanchetta et al., 2007; Magny et al., 2013). However, the potential fluvial contribution from the wider North-African margin is largely unknown.

At sapropel times, intensified monsoon precipitation could reactivate North-African fossil river/wadi systems (presently buried beneath sand dunes), transporting substantial amounts of detrital material and freshwater to the EMS. This scenario has been proposed for sapropel S5 (i.e. MIS 5e, ~125 ka) based on planktonic foraminiferal $\delta^{18}O$, indicating a northward shift of the ITCZ beyond the central Saharan watershed at ~21°N (Rohling et al., 2002, 2004). The inferred runoff from the Saharan mountains is also reflected in Nd isotopes of planktonic foraminifera at the same site, ODP971, off NE Libya (Osborne et al., 2008, 2010) (Fig. 1). Moreover, satellite mapping (Paillou et al., 2009, 2012) as well as paleohydrological and hydraulic modeling (Coulthard et al., 2013) have revealed the existence of paleodrainage networks. These routes into the EMS may have rivaled the Nile runoff in magnitude (Scrivner et al., 2004) and functioned for a majority of Quaternary sapropels (e.g. S1: Krom et al., 1999b; Freydier et al., 2001; S6: Emeis et al., 2003). This hypothesis is also supported by derived dust variations over the past 3 Ma (Larrasoaña et al., 2003, 2013). A similar case has been found off West Africa. The findings of a large submarine canyon (Krastel et al., 2004; Antobreh and Krastel, 2006), deposition of river-borne material (Zühlsdorff et al., 2007; Tjallingii et al., 2008), and the associated subaerial paleodrainage system Tamanrasett (Vörösmarty et al., 2000; Skonieczny et al., 2015) have revealed recurrent fluvial discharge to the Atlantic margin during late-Quaternary sapropel periods (core GeoB7920) (Fig. 1).

Based on Sr and Nd isotopes and supported by major elements, Wu et al. (2016) recently demonstrated that such a scenario occurred also for the Holocene sapropel S1. However, several critical issues about the North-African fluvial contribution remain elusive. Their geochemical and mineralogical composition has not been specified. The transport processes are also unknown: what/how the depositional environment was and whether the detrital supply was accompanied by considerable freshwater inputs. In particular, the origin of such paleodrainage discharge is not clear. With three major paleodrainage systems identified, Coulthard et al. (2013) suggested that the Irharhar flowing over the central Sahara represents the most likely route for human migration out of Africa. Although the Irharhar is mostly non-discharging under the present climate regime, it has been recognized as a large (paleo) river system in the world (Vörösmarty et al., 2000). Moreover, fluvial evidence has been widely inferred from lake and cave deposits as well as anthropogenic sequences over its headwater region (Cremaschi and Zerboni, 2009; Drake et al., 2011; Zerboni et al., 2015). By contrast, the presently buried fluvial networks over eastern Libya (i.e. Kufrah and Sahabi), as revealed by satellite imagery (Paillou et al., 2009, 2012), are reported to be the potential primary deliverers during sapropel S5 deposition (Rohling et al., 2002, 2004; Osborne et al., 2008, 2010) (Fig. 1).

To shed light on this gap in our knowledge, a multiproxy study – coupling major elements, clay minerals, grain-size distribution, and $\delta^{18}O$ of planktonic foraminifera – is employed to distinguish and characterize the terrigenous detrital supplies to the Libyan-Tunisian margin during the last 18 ka. Elemental geochemistry and clay mineralogy of marine sediments have been widely used to track changes in detrital supply over the circum-Mediterranean (Bout-Roumazeilles et al., 2007; Scheuvens et al., 2013; Martinez-Ruiz et al., 2015; and references therein). The end-member modeling technique of Weltje (1997) applied to grain-size distributions is a powerful tool for unmixing of different components in detrital sediments (e.g. Stuut et al., 2002; Hamann et al., 2008; Tjallingii et al., 2008; McGee et al., 2013). Planktonic foraminiferal $\delta^{18}O$ data can indicate freshwater input (e.g. Kallel et al., 1997; Rohling et al., 2002; Hennekam et al., 2014, 2015). In comparison with published results from other core-sites (Fig. 1), we not only constrain the variability of detrital supplies into the central Mediterranean Sea, but also give new insights in the fluvial discharge from the North-African margin, with implications for the mechanism controlling the paleodrainage delivery.

2. Material and methods

Cores CP10BC and CP11PC were collected at the same site (34°32.7′N, 16°34.0′E; 1501 m water-depth) in the SE Ionian Sea, central Mediterranean, during the RV *Pelagia* CORTADO cruise in 2011 (Fig. 1). This site is strategically located at the Libyan-Tunisian slope, underneath the eastward pathway of surface waters, thereby offering a sensitive monitor for the North-African fluvial discharge (Fig. 1a). The 35.5-cm long boxcore CP10BC was sampled every 0.25 cm for geochemical and grain-size analyses, and every 0.5 cm for clay mineral and foraminiferal studies. The description and sampling of core CP10BC was given in Wu et al. (2016). For obtaining the whole sapropel S1 related interval, piston core CP11PC (total length: 10.8 m) was sliced at 0.5 cm intervals for the upper 50 cm. The two cores were correlated using absolute radiocarbon dates and the well-established criteria of sapropel S1 boundaries (10.8–6.1 ± 0.5 ka) (De Lange et al., 2008; see Supplementary material). Hereafter, these combined cores from the same site are referred to as "core CP10/11".

The chronology for core CP10/11 was developed by means of 8 radiocarbon dates on mixed planktonic foraminifers, and 9 measurements of ^{210}Pb and ^{137}Cs on sediment samples. Around 15 mg of mixed planktonic foraminifera (*G. ruber* and *G. sacculifer*) in the 150–600 μm fractions was picked for ^{14}C analyses at the Poznan Radiocarbon Laboratory (Table 1). Inventories and activities of ^{210}Pb and ^{137}Cs on bulk sediments were determined via gamma spectrometry at ENEA, La Spezia (c.f. Barsanti et al., 2011), indicating that the age of CP10BC core-top can be assessed as the present-day (see Supplementary material). Taken together, linear interpolations between the tie-points result in a highly consistent depth-age curve with a basal age of ~18 ka for the sampled CP10/11 intervals (see Supplementary material).

Stable isotopes were analyzed on the sea-surface dwelling foraminifera *G. ruber* (white) (Hennekam et al., 2014). Clean and intact tests were picked from the 250–300 μm size range. Approximately 20–80 μg of foraminifera (i.e. 2–5 shells) was analyzed with a Kiel-III carbonate preparation device connected to a Finnigan MAT-253 mass spectrometer. The average standard deviation for $\delta^{18}O$ is 0.08‰, based on the regular measurements of duplicates and the NBS-19 standard. The *G. ruber* $\delta^{18}O$ ($\delta^{18}O_{ruber}$) values are reported in per mil (‰) relative to the Vienna PeeDee Belemnite (VPDB).

Following the protocol in Van Santvoort et al. (1996), freeze-dried, powdered bulk sediments were decarbonated by shaking in 1 M HCl for 4 + 12 h. Subsequently, the residues were rinsed

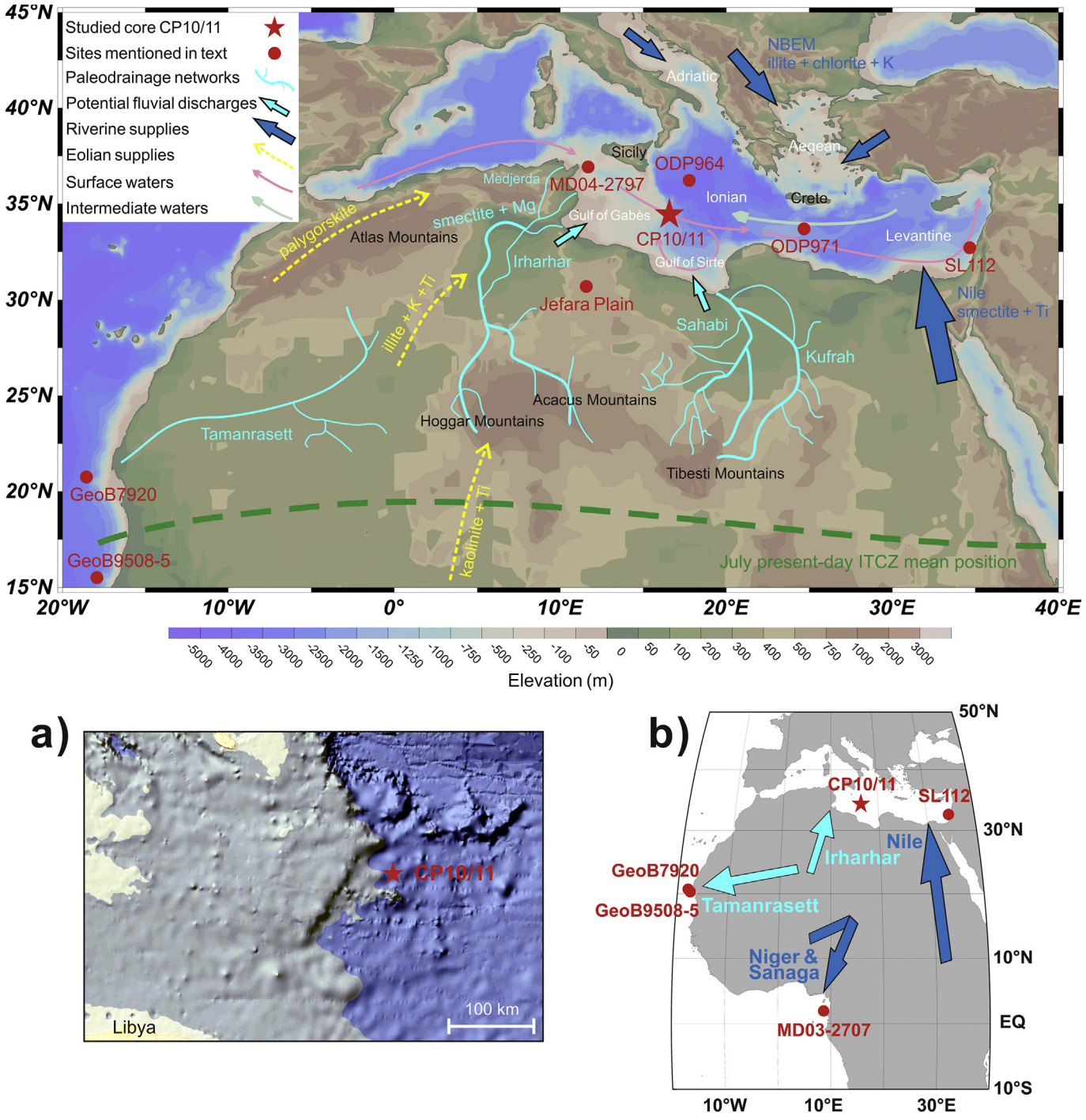

Fig. 1. Topographic map of North Africa and the Mediterranean Sea with a hydrological context, showing the locations of core CP10/11 (red star) and other sites mentioned in text (red circles): MD04-2797 (Essallami et al., 2007; Bout-Roumazeilles et al., 2013), ODP 964 (Zhao et al., 2016), ODP 971 (Rohling et al., 2002, 2004; Osborne et al., 2008, 2010), SL112 (Weldeab et al., 2014), GeoB7920 (Tjallingii et al., 2008; Skonieczny et al., 2015), GeoB9508-5 (Niedermeyer et al., 2010), MD03-2707 (Weldeab et al., 2007), and Jefara Plain (Giraudi et al., 2013). Potential paleodrainage networks derived from central Saharan mountains along the wider North-African margins (i.e. Kufrah, Sahabi, and Irharhar including the Medjerda) are outlined (Vörösmarty et al., 2000; Rohling et al., 2002; Paillou et al., 2009; Coulthard et al., 2013). The Tamanrasett paleodrainage system toward the West-African coast is also drawn (Skonieczny et al., 2015), which has the same headwater region of the Hoggar-Acacus mountains as the Irharhar. The present-day perennial riverine discharges (blue arrows) and major dust emission paths (yellow dotted arrow-headed lines) to the central Mediterranean are indicated. The characteristic signatures for different detrital contributions are labeled (see text). The general circulations of surface-water and of intermediate-water are after Pinardi and Masetti (2000). a) Detailed bathymetric map of the Libyan-Tunisian margin. b) Zoom-out view of the different fluvial discharges, showing core MD03-2707 (Weldeab et al., 2007) receiving the Niger and Sanaga runoff. (For interpretation of the references to colour in this figure legend, the reader is referred to the web version of this article.)

twice with distilled water, oven-dried at 80 °C, and ground. Elemental compositions were analyzed on a Spectro Arcos Inductively Coupled Plasma-Optical Emission Spectroscopy (ICP-OES) after a three-step total digestion (Reitz et al., 2006). Powdered samples were digested in a mixture of HF-$HClO_4$-HNO_3 and heated at 90 °C in a gastight Teflon vessel for at least 12 h. The solution was evaporated at 160 °C to near dryness, and then the residue was dissolved in 4.5% HNO_3 at 90 °C. Reported concentrations were

Table 1
Radiocarbon chronology of core-site CP10/11.

Core	Lab code	Depth (cm)	^{14}C age ± 2σ (yr BP)	Calibrated age ± 2σ (yr cal. BP) [a]
CP10BC	Poz-55177 [b]	6–6.5	2280 ± 30	1893 ± 85
CP10BC	Poz-55178 [b]	18.5–19	5130 ± 40	5486 ± 99
CP10BC	Poz-74802	25.5–26	6920 ± 40	7422 ± 89
CP10BC	Poz-55179 [b]	28–28.5	7330 ± 40	7795 ± 107
CP10BC	Poz-55180 [b]	34–34.5	8770 ± 50	9423 ± 101
CP11PC	Poz-82843	4–4.5	2680 ± 30	2385 ± 85
CP11PC	Poz-74666	30–30.5	11190 ± 60	12691 ± 116
CP11PC	Poz-74667	47–47.5	14530 ± 70	17201 ± 253

[a] Using Marine13 calibration curve (Reimer et al., 2013), implemented in program Calib 7.0 (Stuiver and Reimer, 1993), with no regional offset (ΔR = 0) (Siani et al., 2000).
[b] Data from Wu et al. (2016).

determined on the carbonate-free samples, thus representing the non-biogenic, "detrital" sediment alone, except for the Ba/Al data that are for bulk sediment samples. Analytical uncertainties were monitored by blanks, duplicates, and standards (ISE 921), showing that accuracy is better than 6% and precision better than 3% for all targeted elements. Given its conservative behavior, Al is adopted for normalizations here to assess the relative enrichment/depletion of specific elements (c.f. Martinez-Ruiz et al., 2015).

Clay minerals were identified by X-ray diffraction (XRD) using a PANalytical X'Pert Pro diffractometer, with a 0.03°2Θ/s rate under CuKα radiation and Ni filter, at Tongji University (Wu et al., 2012; Schroeder et al., 2015). The analysis was conducted on oriented mounts of non-calcareous, clay-sized particles (<2 μm), which were obtained after the protocol described by Liu et al. (2004). The XRD runs were performed under three conditions: untreated, glycolated (in ethylene-glycol vapor for 24 h), and heated (490 °C for 2 h). Identification of clay minerals was done according to a comprehensive comparison of the three XRD diagrams. For the main clay-mineral groups, the relative abundances were calculated by measuring the peak areas on glycolated curve using MacDiff 4.2 software (Petschick, 2000); i.e. smectite (including mixed layers) (15–17 Å), illite (10 Å), and kaolinite/chlorite (7 Å). Relative proportions of kaolinite and chlorite were determined using the ratio of 3.57/3.54 Å peak areas. Palygorskite (10.6 Å) was also detected. Following the laboratory routine, the weighing factors introduced by Biscaye (1965) are not applied. Additionally, illite parameters were calculated to track provenance (Petschick et al., 1996). On the glycolated curve, the illite chemistry index refers to the ratio of the 5 Å and 10 Å peak areas, and illite crystallinity was obtained from half height width of the 10 Å peak. The reproducibility error of this method is <5%.

For grain-size analyses of the detrital fraction, bulk sediment was treated with 10% H_2O_2 at 80 °C using a water-bath, until reaction stopped to remove organic matter, and subsequently with 1 M HCl for 6 h to remove marine carbonates. Microscope observations confirmed that this procedure successfully eliminated all biogenic constituents. After boiling briefly with a dispersing agent ($Na_4P_2O_7$), the CP10BC and CP11PC samples were measured on the Malvern Mastersizer-S and -2000 instruments, respectively, resulting in 64 size classes (0.06–879 μm) (Stuut et al., 2002). As the very fine fraction (<0.5 μm) has no meaning sedimentologically and accounts for a negligible proportion, the number of input variables is routinely reduced to 49 size classes (0.5–879 μm) for the subsequent end-member modeling (c.f. Stuut et al., 2002). The end-member modeling algorithm (EMMA) of Weltje (1997) is used to decompose the measured grain-size distribution into proportional contributions of an optimal set of end members (i.e. EMs). The inversion algorithm approximates a theoretical grain-size distribution by iterative calculation of the least-square fit between the measured grain-size distribution and the mixture of the calculated EMs. To estimate the minimum number of EMs required for a satisfactory approximation of the data (n = 141), the

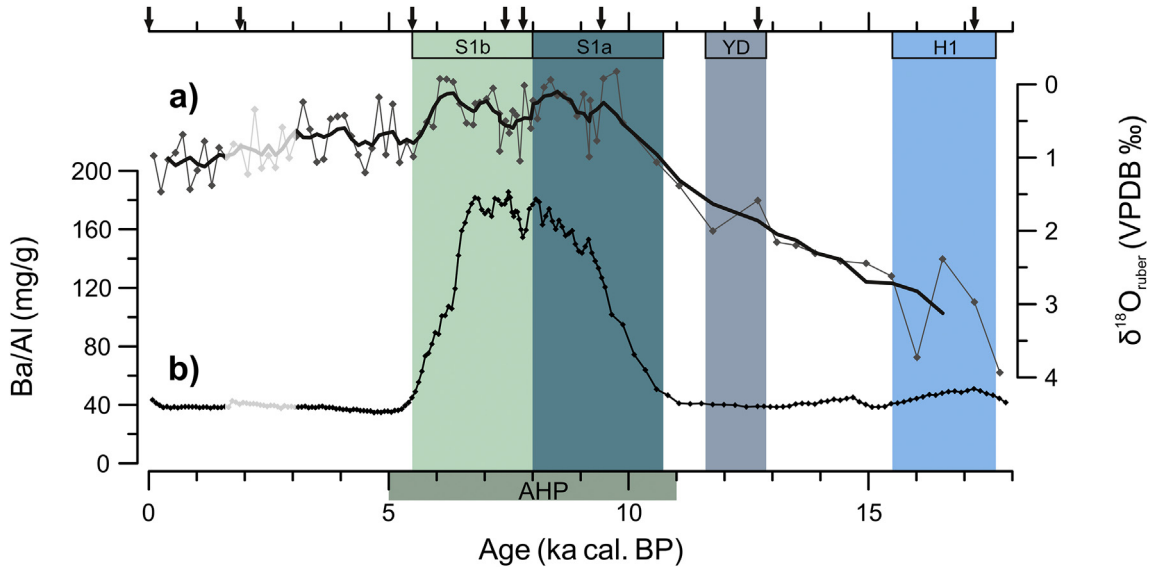

Fig. 2. Geochemical records for core CP10/11 over the past 18 ka. a) Planktonic foraminiferal *G. ruber* δ^{18}O, with 5-point moving average superimposed. b) Ba/Al of bulk sediment basis (Wu et al., 2016). Age tie-points are indicated by arrows at the upper axis. The tephra-related interval (~3.0–1.5 ka) mentioned in Section 3.1 is disregarded in this contribution. Sapropel S1a and S1b intervals, Heinrich event 1 (H1), Younger Dryas (YD), and African Humid Period (AHP) are specified (see Section 3).

coefficients of determination (r^2) of each size class, and the mean coefficient of determination (r^2_{mean}) were calculated. These coefficients represent the proportion of variance that can be reproduced by the approximated data (Weltje, 1997).

3. Results

3.1. G. ruber $\delta^{18}O$ and bulk Ba/Al

The $\delta^{18}O_{ruber}$ record in core CP10/11 shows a shift from enriched values (~4‰) around the Heinrich event 1 (H1), to much more depleted values of ~0.5‰ at ~10 ka. The profile maintains the depleted $\delta^{18}O_{ruber}$ ratios over the AHP, followed by a gradual increase to ~1‰ today (Fig. 2a). As post-depositional oxidation removed most of the organic carbon, but not the co-settling biogenic Ba from the upper-most part of sapropels, the full extent of sapropel S1 is recognized by the elevated zone of bulk Ba/Al (Van Santvoort et al., 1996; De Lange et al., 2008). For core CP10/11 this is between ~10.8 and 5.8 ka (Fig. 2b), in agreement with previous studies (~10.8–6.1 ± 0.5 ka) (c.f. De Lange et al., 2008). Sapropel S1, largely coeval with the AHP, can be split into S1a and S1b periods, divided by the 8.2 ka interruption, visible here in Ba/Al at ~8.2–7.8 ka (Rohling and Pälike, 2005; Wu et al., 2016). The sedimentation rates are between 2.8 and 4.1 cm/ka, and is relatively high during the S1 period, S1b in particular, and lower for the arid intervals (Wu et al., 2016) (see Supplementary material).

The interval of ~3.0–1.5 ka is affected by dispersed tephra as identified in several samples (Wu et al., 2016), thus we will disregard this interval from hereon. In the following, data are grouped into four different periods of sediment transport and deposition: pre-AHP (~18.0–10.8 ka), S1a (~10.8–8.0 ka), S1b (~8.0–5.5 ka), and post-AHP (~5.5–0 ka).

3.2. Grain size end-member modeling

The mean grain-size distribution of core CP10/11 has a modal value near 5 μm (Fig. 3a). For the total set of distributions (n = 141), the coefficients of determination (r^2) are plotted against grain size for models with 2–10 EMs (Fig. 3b). The mean coefficient of determination (r^2_{mean}) of the grain-size classes increases when the

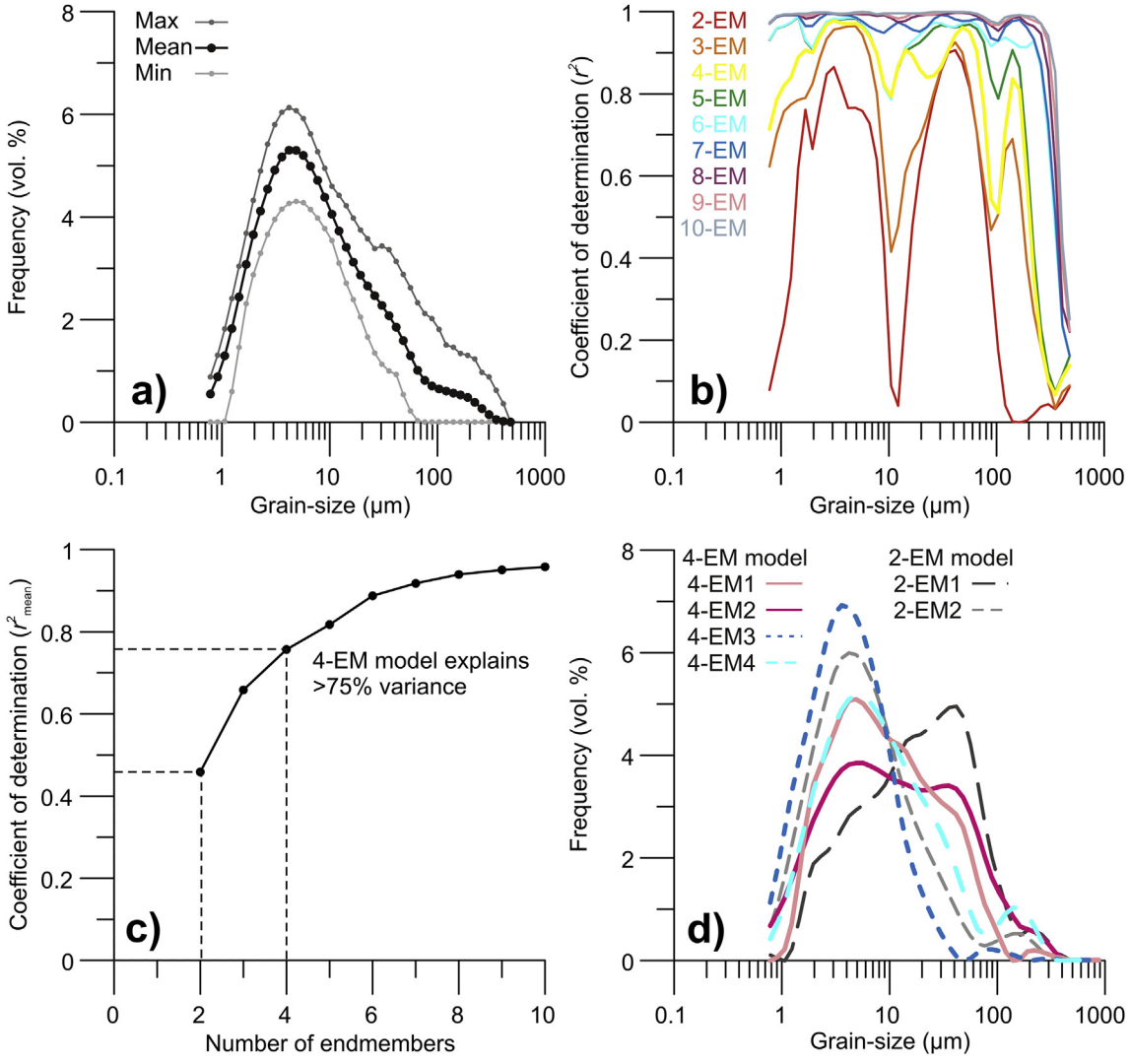

Fig. 3. End-member modeling results of core CP10/11 grain-size data. a) Summary statistics of raw data (n = 141); maximum, mean, and minimum frequency recorded in each size class. b) Coefficients of determination (r^2) per size class for models with 2–10 end members. c) Mean coefficient of determination (r^2_{mean}) of all size classes for each model. d) Modeled grain-size distributions of end members for the 4-EM and 2-EM models. The goodness-of-fit statistics suggest that the 4-EM model is an adequately reliable choice (see Section 3.2). Data of the tephra-related interval (~3.0–1.5 ka) were removed for the modeling (see Section 3.1).

number of EMs increases (Fig. 3c). End-member modeling (EMMA) of the CP10/11 grain-size data results in two contrasting components in the 2-EM model (i.e. the model with 2 end members; and so on), which are consistent with the varying climatic conditions (Figs. 3d and 4b). However, this model has a low r^2_{mean} (0.46) and especially low r^2 (<0.4) for the ranges of ~10–16 μm and >90 μm (Fig. 3b,c). The 3-EM model reports a higher but still unsatisfactory fit ($r^2_{mean} = 0.66$). The 4-EM model explains more than 75% of the variance in the total dataset, and considerably improves the ranges of ~10–16 μm ($r^2 > 0.8$), and of ~90–200 μm ($r^2 = 0.5–0.8$) to an

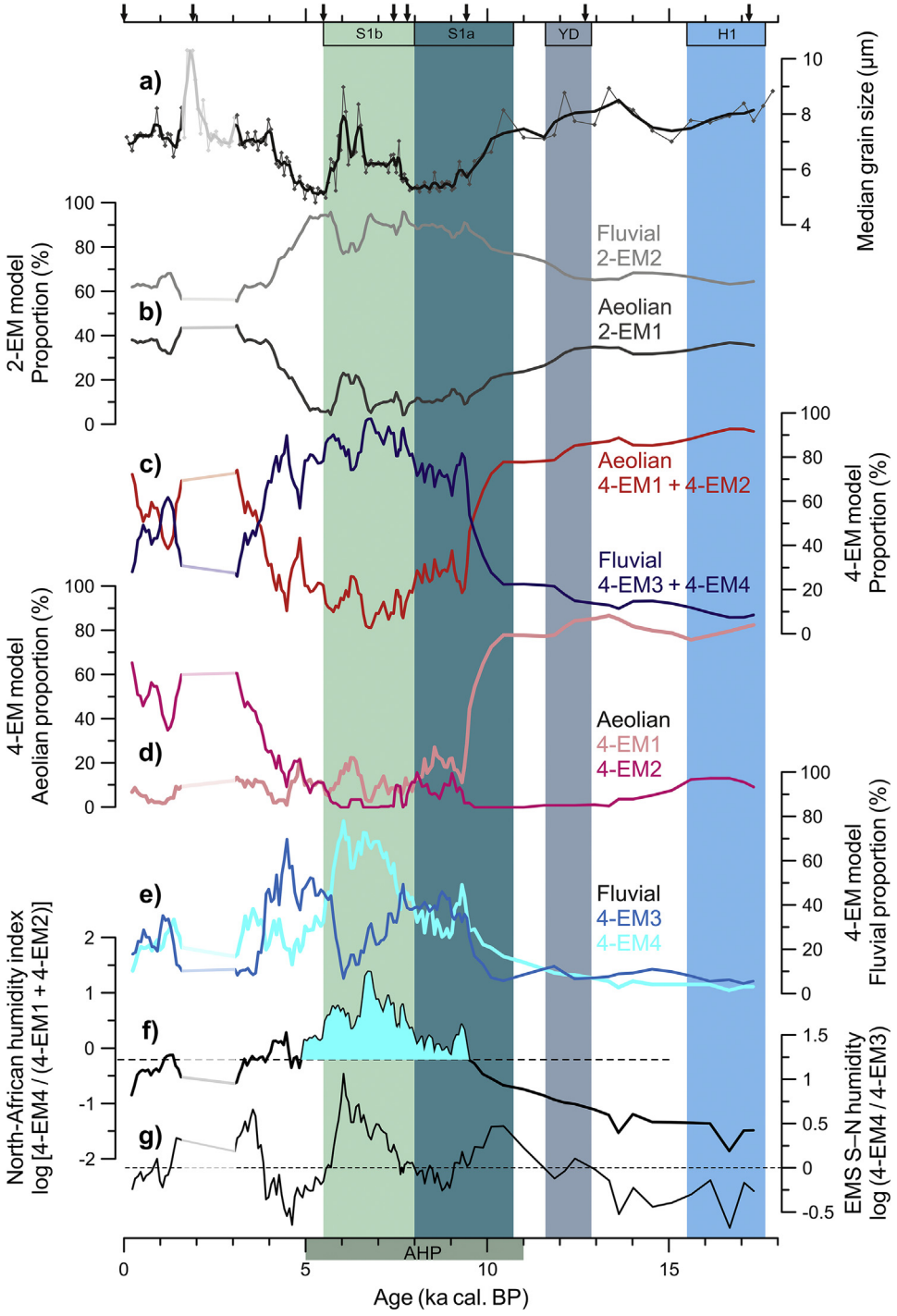

Fig. 4. Grain-size records for core CP10/11 over the past 18 ka. a) Median grain size of detrital particles, with 3-point moving average superimposed. Aeolian and fluvial components presented in b) 2-EM model and c) 4-EM model, respectively. d) Proportions of aeolian end members for 4-EM model, which dominated the arid periods before (4-EM1) and after (4-EM2) sapropel S1, respectively. e) Proportions of fluvial end members for 4-EM model, which are interpreted to indicate the NBEM riverine inputs and the North-African paleodrainage discharges, respectively. f) Continental humidity index of North Africa, expressed as a log-ratio of the North-African fluvial (4-EM4) and aeolian (4-EM1 + 4-EM2) end members. g) Log-ratio of the North-African (4-EM4) and the NBEM riverine (4-EM3) fluvial end members, is thought to reflect relative S–N humidity of the eastern Mediterranean. Note that the grain-size modeled data are reported as 5-point moving average. Age tie-points are indicated by arrows at the upper axis. The tephra-related interval (~3.0–1.5 ka) is disregarded (see Section 3.1). Sapropel S1a and S1b intervals, Heinrich event 1 (H1), Younger Dryas (YD), and African Humid Period (AHP) are specified (see Section 3).

adequate extent (Fig. 3b,c). The coarse tail (>90 μm) can only be sufficiently addressed with ≥5 EMs, but this fraction can be ignored because it comprises <4% of the total weight-mass of the samples (Fig. 3b). This is justified by 1) the limited improvement of the goodness-of-fit with the use of ≥5 EMs and 2) the clear separation of aeolian supplies that mainly occupy the coarse-particle fraction by using a 4-EM model (Figs. 3d and 4b). By contrast, the range of ~10–16 μm should be well reproduced by the mixing model, as this range contains a large proportion of the total mass. In brief, the goodness-of-fit statistics, combined with the grain-size distributions of the EMs, demonstrate that the 4-EM model provides the best balance between minimum number of EMs and maximum r^2.

Accordingly, the modeled grain-size distribution (Fig. 3d) and downcore variability (Fig. 4b–e) of the EMs are shown for the 4-EM model, with those of the 2-EM model for comparison. The end member 2-EM1 (i.e. the 2-EM model's 1st end member; and so on) has a dominant mode of ~40 μm, and 2-EM2 of ~4 μm (Fig. 3d). For the 4-EM model, all end members have a well-defined distribution. The 4-EM1 has a major peak near 6 μm, with two minor bulges at ~12 and 40 μm. The 4-EM2 shows a poorly sorted, bimodal distribution with modes at ~6 and 35 μm. The 4-EM3 has a well sorted, dominant mode at ~3 μm. The 4-EM4 shows a modal grain size of ~5 μm, and a minor peak near 150 μm (Fig. 3d).

The median grain size in core CP10/11 varies between 4 and 11 μm, displaying generally lower values during the AHP, except for the S1b interval (Fig. 4a). Likewise, the 2-EM1 proportion is lower during the AHP; and vice versa for 2-EM2 (Fig. 4b). Two different components (i.e. 4-EM1 + 4EM-2, 4-EM3 + 4EM-4) are clearly presented in the 4-EM model (Fig. 4c). A high proportion (~80%) of 4-EM1 occurs only before sapropel S1, whereas the 4-EM2 proportion steadily increases up to 80% after the AHP (Fig. 4d). An enhanced proportion of 4-EM3 corresponds with the Ba/Al within sapropel S1 (~10–6 ka), followed by a peculiar increase around 5 ka. The 4-EM4 also shows elevated contributions during the AHP, but is different from 4-EM3 in variability. The 4-EM4 proportions are highest during S1b, in contrast to the simultaneously decreasing trend observed for 4-EM3 (Fig. 4e). Moreover, humidity indexes are calculated for the North-African continent and eastern-Mediterranean region (after Tjallingii et al., 2008) (Fig. 4f,g; see Section 4.3).

3.3. Detrital elemental ratios and clay minerals

The Ti/Al ratio is recognized as a proxy for Saharan dust, while higher values of K/Al and detrital Mg/Al are generally interpreted as enhanced fluvial inputs to the EMS (Wehausen and Brumsack, 2000; Martinez-Ruiz et al., 2015, and references therein). In core CP10/11, the Ti/Al record displays a descending trend from H1 to the Younger Dryas (YD), with relatively low values for S1a. The Ti/Al reaches a minimum value at ~6.5 ka, followed by a steady increase (Fig. 5a). The K/Al profile displays a similar evolution as that of Ti/Al before the AHP, but differs in two aspects for the Holocene: 1) having generally higher values in the AHP and 2) reaching the lowest value much later (~5 ka) (Fig. 5b). The Mg/Al record shows very distinctive changes. After a slight decrease from H1 to YD, Mg/Al increases and shows the highest value during the S1b, followed by a decline till the present (Fig. 6e). Additionally, transition elements Ni and Cr are typically concentrated in mafic igneous rocks, and thus high Ni/Al and Cr/Al suggest more mafic provenance (c.f. Wu et al., 2013). The Ni/Al and Cr/Al profiles show close relationships with Mg/Al (Fig. 6e–g).

The clay-mineral assemblage of core CP10/11 over the past 18 ka is composed of dominant smectite (42–56%), moderate kaolinite (16–25%) and illite (15–21%), and minor chlorite (8–13%) and palygorskite (1–3%). The major clay minerals exhibit striking similarities to elemental ratios, i.e. smectite – Mg/Al (Fig. 6e,h), kaolinite – Ti/Al (Fig. 5a,c), and illite – K/Al (Fig. 5b,e) (see Section 4). Chlorite is generally higher (lower) during the period before (after) ~8 ka (Fig. 5g), while the palygorskite has low values and displays no discernible pattern (Fig. 6l). The illite to kaolinite (I/K) ratio varies within a narrow range before ~10 ka; after a slight increase during S1a, a steady decline occurs (Fig. 5i). The chlorite to kaolinite (C/K) and smectite/kaolinite (S/K) ratios have a variability similar to that of I/K, but with a more pronounced increase during S1a for C/K and more enhanced values during S1b for S/K (Figs. 5k and 6j).

3.4. Estimated elemental ratios of grain-size end members

Via combining the results of grain size end-member modeling, with the elemental data, which are both derived from the detrital sediment fraction, a quantitative estimation of the elemental fingerprints for the 4-EM end members was made. For a certain element, the Al-normalized ratios were calculated using the equation: $\text{Element/Al}_{\text{sample}} = \text{Proportion}_{4\text{-EM1}} \times \text{Element/Al}_{4\text{-EM1}} + \text{Proportion}_{4\text{-EM2}} \times \text{Element/Al}_{4\text{-EM2}} + \text{Proportion}_{4\text{-EM3}} \times \text{Element/Al}_{4\text{-EM3}} + \text{Proportion}_{4\text{-EM4}} \times \text{Element/Al}_{4\text{-EM4}}$, where $\text{Element/Al}_{\text{sample}}$ is the measured elemental ratio in detrital sediment, $\text{Proportion}_{4\text{-EM1}}$ is the proportion of end member 4-EM1 (and so on), and $\text{Element/Al}_{4\text{-EM1}}$ is the (unknown) elemental ratio of end member 4-EM1 (and so on). This equation was applied for the four periods with different climatic conditions (i.e. pre-AHP, S1a, S1b, and post-AHP). Thus with four equations, the unknown elemental ratios for the four end members can be determined. Note that the proportions of grain-size end members and the measured elemental ratios are taken as average values for a certain interval. This calculation was done for the three characteristic elements (i.e. Ti, K, and Mg). The results are presented in Table 2.

4. Discussion

A strong west–east gradient has been reported for surface sediments in the EMS, caused by mixing between two end members: Saharan dust vs. Nile sediments (Venkatarathnam and Ryan, 1971; Krom et al., 1999a; Weldeab et al., 2002a). This two-end-member model is usually adequate to explain the variability of sediment composition in the eastern section of the EMS (e.g. Krom et al., 1999b; Wehausen and Brumsack, 2000; Freydier et al., 2001; Weldeab et al., 2002b; Revel et al., 2010). For the central Mediterranean, however, detrital sediments can only be assigned to a ternary mixing system based on Sr and Nd isotopes, including 1) Saharan dust, 2) riverine inputs from the Nile and NBEM (i.e. Northern Borderlands of the Eastern Mediterranean), and 3) fluvial/shelf-derived fluxes from the Libyan-Tunisian margin (Wu et al., 2016). Therefore, although there is a general agreement on the overall systematics and provenance, several important controversies and unresolved issues remain:

1) Sources of Saharan dust are not evenly distributed over North Africa, have different elemental and mineralogical composition and may change substantially through time (Krom et al., 1999a; McGee et al., 2013; Scheuvens et al., 2013).
2) Riverine inputs from the NBEM and Nile have a similar Sr-Nd isotopic signature, thus cannot be differentiated using these isotopes alone (Weldeab et al., 2002a, 2002b; Wu et al., 2016).
3) Past detrital supply from the Libyan-Tunisian margin is poorly known for its composition and origin (see Section 1).

The complex controls on the provenance of central-Mediterranean sediments urge for a multi-proxy approach. We have done so on the well-dated CP10/11 core. The EMMA technique (Weltje, 1997) is applied to the grain-size data to distinguish

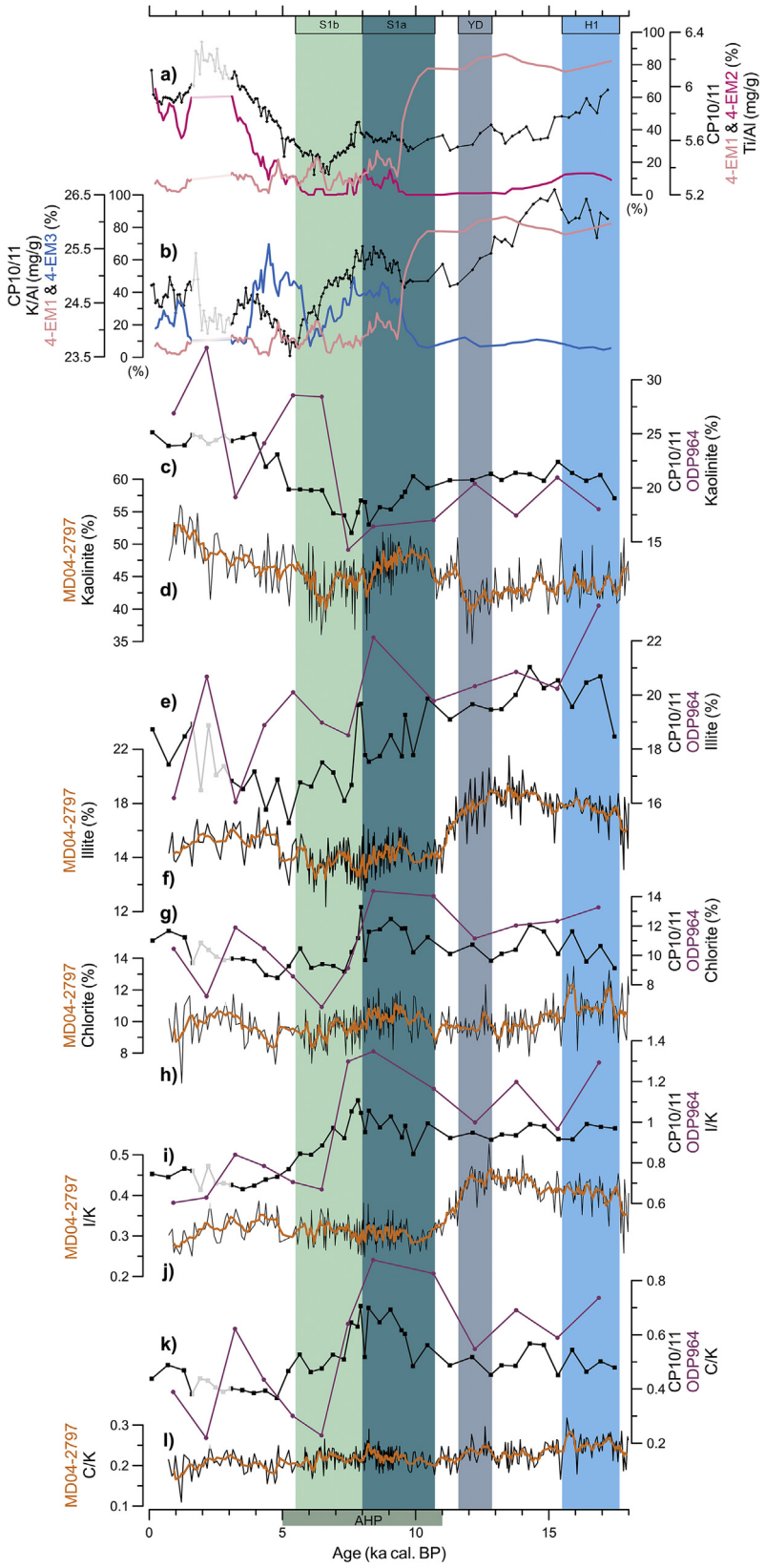

Fig. 5. Comparison of detrital records between cores CP10/11, MD04-2797 (Bout-Roumazeilles et al., 2013), and ODP964 (Zhao et al., 2016) to distinguish aeolian and riverine supplies. a) Ti/Al (black), and proportions of Saharan dust end members 4-EM1 (pink) and 4-EM2 (magenta) in CP10/11. b) K/Al (black), and proportions of aeolian end member 4-EM1 (pink) and of NBEM riverine end member 4-EM3 (blue) in CP10/11. c) Kaolinite for CP10/11 and ODP964. d) Kaolinite in MD04-2797. e) Illite for CP10/11 and ODP964. f) Illite in MD04-2797. g) Chlorite for CP10/11 and ODP964. h) Chlorite in MD04-2797. i) I/K (illite/kaolinite) for CP10/11 and ODP964. j) I/K in MD04-2797. k) C/K (chlorite/kaolinite) for CP10/11 and for ODP964. l) C/K in MD04-2797. The profiles of grain-size derived data are reported as 5-point moving average. Note that the elemental and clay mineralogy records of CP10/11 are shown in black, ODP964 records in purple, and 5-point moving average (orange line) is also superimposed for MD04-2797. The tephra-related interval (~3.0–1.5 ka) is disregarded (see Section 3.1). Sapropel S1a and S1b intervals, Heinrich event 1 (H1), Younger Dryas (YD), and African Humid Period (AHP) are specified (see Section 3). (For interpretation of the references to colour in this figure legend, the reader is referred to the web version of this article.)

aeolian and fluvial contributions. Different contributions are further characterized using major elements, clay minerals, and foraminiferal $\delta^{18}O_{ruber}$. In this way, the sediment provenance, especially for the North-African paleodrainage runoff, is unraveled. In a wider perspective, we compare our data with those published for cores MD04-2797 at the Strait of Sicily (Essallami et al., 2007; Bout-Roumazeilles et al., 2013), ODP964 in the Ionian Sea (Zhao et al., 2016), and GeoB7920 off West Africa (Tjallingii et al., 2008; Skonieczny et al., 2015). Finally, we discuss our findings in relation to paleo-hydroclimate changes over North Africa.

4.1. Distinguishing aeolian and riverine inputs to the central Mediterranean

Terrigenous detrital deposits on continental margins represent mixtures of components brought in by wind and delivered by rivers. For the CP10/11 grain-size data, two contrasting components are generated by the 2-EM model, i.e. 2-EM1 is interpreted as aeolian and 2-EM2 as fluvial sediments (Figs. 3d and 4b). Similarly but much more distinctly, aeolian (4-EM1 + 4EM-2) and fluvial (4-EM3 + 4EM-4) contributions are characterized by the 4-EM model, showing that their variation corresponds with the AHP-associated arid and humid conditions (Fig. 4c).

The grain size of aeolian particles deposited in deep-sea sediments depends on the distance to the source and the capacity of the transporting agent. Aeolian contributions to deep-sea sediments are usually coarser grained than riverine, hemipelagic components. As a result, terrigenous detrital particles with a median grain size >6 μm are generally attributed to aeolian transport, and hemipelagic deposition is often assumed for the <6 μm particles. This is based on deep-sea sediment studies (e.g. Sarnthein et al., 1981; Sirocko et al., 1991; Prins et al., 2000) as well as modern-dust studies during which dust was collected at sea in various areas (e.g. Clemens, 1998; Ratmeyer et al., 1999; Stuut et al., 2005). Moreover, this concept has often been adopted to tentatively separate the eolian and fluvial contributions (e.g. Stuut et al., 2002; Tjallingii et al., 2008; McGee et al., 2013).

Here, our 4-EM1 and 4-EM2 are considered to be of aeolian origin, and the 4-EM3 and 4-EM4 are thought to be hemipelagic (Figs. 3d and 4c). Specifically, the aeolian character of 4-EM1 and 4-EM2 is corroborated by their downcore variations, displaying high proportions only during non-AHP intervals dominated by an arid Saharan regime (Fig. 4d). The enhanced contributions of 4-EM3 and 4-EM4 during the AHP are interpreted as non-aeolian hemipelagic mud associated with fluvially transported material (Fig. 4e). As discussed below, we will examine these interpretations combined with the results of detrital elements and clay minerals.

4.1.1. Saharan dust

Today Saharan dust is the dominant component of central-Mediterranean sediments (Guerzoni et al., 1997; Rutten et al., 2000; Scheuvens et al., 2013). Dust from the northern and eastern borderlands of the Mediterranean is quantitatively negligible (Guerzoni et al., 1997; Ehrmann et al., 2007). Because Ti principally resides in heavy minerals and is enriched in modern Saharan aerosols, the Ti/Al ratio has been widely used as a proxy for Saharan dust (e.g. Wehausen and Brumsack, 2000; Lourens et al., 2001; Wu et al., 2016). Part of the variability of Ti/Al may also result from a change in the grain size of aeolian particles, related to wind strength (Sarnthein et al., 1981; Stuut et al., 2002).

Illite and kaolinite together are reported to constitute a large fraction (usually >50%) of the clay-mineral assemblages of Saharan dust (Guerzoni et al., 1997; Scheuvens et al., 2013). Due to the different efficiency of weathering processes in soils at different latitudes, illite, usually enriched in K, is dominant in the NW sector of the Sahara. By contrast, abundant kaolinite is found at low latitudes, being preferentially formed under humid and warm conditions. As shown in the compilation by Scheuvens et al. (2013), these result in illite (kaolinite) contents for North-African soils to decrease (increase) southward. Furthermore, the I/K ratio in mineral dust exhibits a slight W–E decreasing gradient over North Africa and is considered to be conservative during long-range transport (Caquineau et al., 1998). Consequently, the I/K ratio has been used as a dust-source indicator for the tropical Atlantic (Caquineau et al., 1998; Skonieczny et al., 2013) and the Mediterranean (Bout-Roumazeilles et al., 2007, 2013; Zhao et al., 2016).

In core CP10/11, the evolution of Ti/Al, K/Al, kaolinite, and illite all show a similar pattern, with higher values during non-AHP intervals (Fig. 5a,b,c,e). Given that these aeolian parameters are derived from different size fractions, this suggests that the coherent changes therein mainly result from dust fluxes. Variations in dust flux have been attributed to Saharan lake surface area and vegetation cover (e.g. Claussen et al., 1999; deMenocal et al., 2000; Cockerton et al., 2014; Armitage et al., 2015; Egerer et al., 2016). Indeed, during the AHP, North Africa was perennially covered by dense vegetation and extensive fluvial systems, leading to 70–80% lower dust emissions than today (deMenocal et al., 2000; McGee et al., 2013; Egerer et al., 2016).

4.1.1.1. Pre- and post-AHP dust. Aeolian contributions in core CP10/11 are neatly separated in terms of grain-size distribution. Different supplies of Saharan dust dominate during the pre-AHP (4-EM1) and post-AHP (4-EM2) (Fig. 4d). In fact, for various parameters there is a difference in value before and after the AHP, observed for cores CP10/11, ODP964, and MD04-2797 (Fig. 5a–f). The post-AHP dust seems to have a larger contribution of coarse components and has a higher Ti/Al. Moreover, compared to the pre-AHP, the post-AHP dust contains more kaolinite and less illite. The resulting I/K ratio explicitly indicates a more predominant NW-Saharan dust source for the pre-AHP, and a more SE-Saharan oriented provenance for the post-AHP (Fig. 5i,j). Considering the poor sorting of the aeolian EMs (Fig. 3d), Saharan dust deposited in the central Mediterranean is thought to be multiple-sourced, likely to have proximal and distal contributions. The presence of palygorskite is diagnostic for dust derived from NW Africa (i.e. Morocco, Algeria, and Tunisia) (Bout-Roumazeilles et al., 2007; Scheuvens et al., 2013; Skonieczny et al., 2013). Given the low contents and lack of clear trends in variability for palygorskite (Fig. 6l), the dust from these proximal regions must be minor, but may be persistently active. Taken together, for the pre-AHP compared to the post-AHP interval, our clay-mineral data refer to a more NW-Saharan provenance, while the smaller grain size of the dominant 4-EM1 and the lower Ti/Al values may signify a longer distance to dust sources or weaker wind strength.

Our I/K data for the non-AHP samples generally match with the domain of southern Algeria and Mali, one of the major dust production areas in North Africa nowadays (Bout-Roumazeilles et al., 2007; Scheuvens et al., 2013). However, it must be realized that although kaolinite is considered as a predominantly eolian signal (Venkatarathnam and Ryan, 1971; Bout-Roumazeilles et al., 2007), part of the illite may also originate from non-dust sources. Using I/K alone, this provenance domain is thus difficult to attribute with more certainty.

4.1.1.2. Contrasting AHP versus non-AHP. During the AHP and the nearly coincident sapropel S1, the dust contribution is small, whereas riverine inputs, and associated enhanced illite and K/Al, are more dominant. The decline of the I/K ratio after the YD observed for the Strait of Sicily and on the Iberian shelf (Stumpf et al., 2011), has been attributed to a southward shift of the Saharan dust sources, caused by a southward migration of the ITCZ

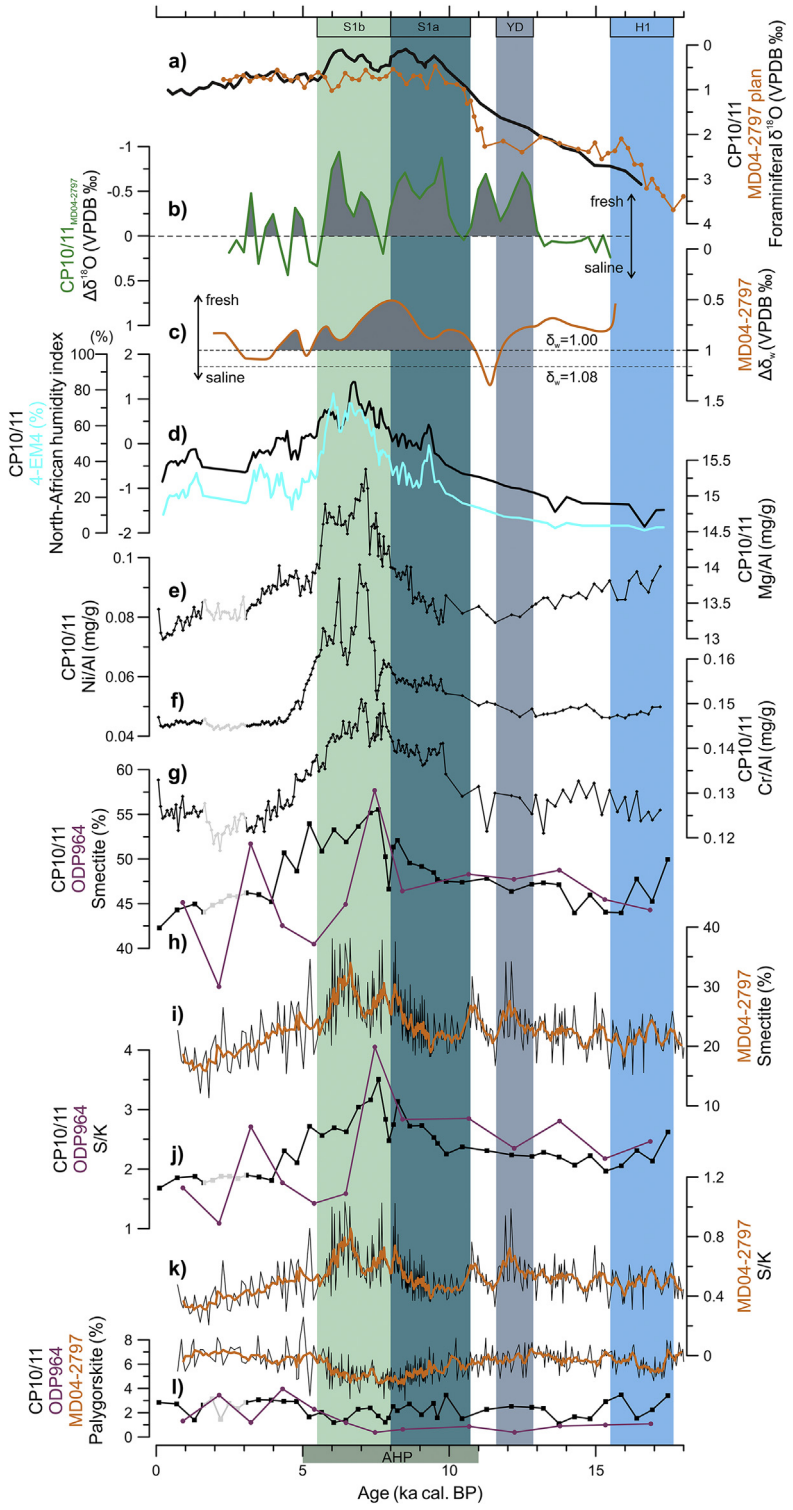

Fig. 6. A tight correspondence between various proxy records from cores CP10/11, MD04-2797 (Essallami et al., 2007; Bout-Roumazeilles et al., 2013), and ODP964 (Zhao et al., 2016) indicates the reactivated paleodrainage systems (mainly Irharhar) along the Libyan-Tunisian margin transported considerable Mg- and smectite-rich detrital materials and freshwater into the Gulf of Gabès. Such fluvial discharge is strongest during the late-AHP, S1b interval (~8.0–5.5 ka), related to an enhanced fluvial dynamics and the most humid conditions in western Libya and Tunisia/Algeria. a) Planktonic foraminiferal $\delta^{18}O$ of *G. ruber* for CP10/11 (black, 5-point moving average) and of *G. bulloides* for MD04-2797 (orange). b) Difference of planktonic foraminiferal $\delta^{18}O$ ($\Delta\delta^{18}O$) between CP10/11 and MD04-2797, i.e. lower value is thought to indicate more freshwater supply to CP10/11 relative to MD04-2797; data were resampled at 250-yr resolution for calculation. c) $\Delta\delta_w$ for MD04-2797, a proxy for salinity, calculated using alkenones-derived SST; modern and S1 background δ_w (local seawater $\delta^{18}O$) values of 1.08 and 1.00 are shown (dash lines). d) Proportion of end member 4-EM4 (cyan), indicative of North-African paleodrainage discharge; North-African humidity index, expressed as a log-ratio of the North-African fluvial and aeolian end members in CP10/11. e) Detrital Mg/Al in CP10/11. f) Ni/Al in CP10/11. g) Cr/Al in CP10/11. h) Smectite for CP10/11 and ODP964. i) Smectite in MD04-2797. j) S/K (smectite/kaolinite) for CP10/11 and ODP964. k) S/K in MD04-2797. l) Palygorskite for CP10/11, ODP964, and MD04-2797. The profiles of grain-size derived data are reported as 5-point moving average. Note that the elemental and clay mineralogy records of CP10/11 are shown in black, ODP964 and MD04-2797 (5-point moving average) records are in purple and orange, respectively. The tephra-related interval (~3.0–1.5 ka) is disregarded (see Section 3.1). Sapropel S1a and S1b intervals, Heinrich event 1 (H1), Younger Dryas (YD), and African Humid Period (AHP) are specified (see Section 3). (For interpretation of the references to colour in this figure legend, the reader is referred to the web version of this article.)

Table 2
Estimated elemental ratios of the grain-size end members for core CP10/11 [a].

Modeled grain-size end members	Ti/Al (mg/g)	K/Al (mg/g)	Mg/Al (mg/g)
4-EM1	5.71	26.2	13.7
4-EM2	6.52	23.4	13.8
4-EM3	5.47	25.8	10.1
4-EM4	5.46	23.8	17.2

[a] For calculation refers to Section 3.4.

(Bout-Roumazeilles et al., 2013). Cores CP10/11 and ODP964 in the Ionian Sea display a similar variability, but with a much delayed decrease, i.e. after S1a (Fig. 5i,j). The different timing can be attributed to the influences of enhanced NBEM riverine inputs (enriched in illite and chlorite) during S1a on cores CP10/11 and ODP964, but not for MD04-2797 (Fig. 5e–h; see Section 4.1.2).

The different illite sources for the Ionian Sea can be discriminated by mineralogical parameters. Lower values of illite chemistry index and illite crystallinity both indicate a weaker chemical hydrolysis formation, and thus a higher latitude environment; and vice versa (Petschick et al., 1996; Zhao et al., 2012, 2016). Accordingly, the high values for chemistry index and crystallinity of illite in non-AHP sediments correspond to the more humid and warm conditions of its formation in subtropical regions, and subsequent transportation as Saharan dust. By contrast, the low values for the illite parameters in the AHP samples point to a high-latitude illite source, characterized by relatively arid and cold conditions (i.e. NBEM riverine inputs) (Fig. 7).

4.1.2. NBEM riverine inputs

Clay-sized particles represent the major component transported by rivers to the Mediterranean Sea. During the late-Quaternary, the Nile sediment is mainly derived from Cenozoic basaltic rocks in the Ethiopian Highlands. This is reflected in the characteristic elemental compositions (high Ti, low K and Mg) (e.g. Krom et al., 1999a, 1999b; Hennekam et al., 2014) and the overwhelming smectite in clay-mineral assemblages of the Nile sediments (e.g. Venkatarathnam and Ryan, 1971; Hamann et al., 2009; Zhao et al., 2012). The Sr and Nd isotopes in surface sediments reveal that the recent Nile contribution rapidly decreases westward from the river-mouth to being negligible south of Crete (Krom et al., 1999a; Weldeab et al., 2002a).

Substantially enhanced sedimentation rates during sapropel S1 occurred only for cores taken within/near the Nile delta (Hennekam et al., 2015). This indicates that during the AHP the offshore spread of Nile sediments was not larger than before or after. Meanwhile, observations of the detrital Sr- and Nd-isotopes and concentrations on leachable and residual fractions of sapropel S1 sediments, taken from cores along a west–east transect throughout the EMS, show that the enhanced Nile discharge (i.e. dissolved and particulate) can only be detected westward until south of Crete (Krom et al., 1999b; Freydier et al., 2001). In accordance, the compositional variability of Ti and K data in core CP10BC clearly indicates a minor–if any–Nile contribution to the central Mediterranean during sapropel S1 (Wu et al., 2016). Taking all evidence together, this means that for the central Mediterranean no appreciable Nile contribution can be expected and in any case there will be no difference for sapropel and non-sapropel periods.

The NBEM is considered an important contributor of illite and chlorite to the Ionian Sea, mainly via rivers flowing into the Adriatic Sea (Po and other rivers) and Aegean Sea (southeastern European and Turkish rivers) (Venkatarathnam and Ryan, 1971; Guerzoni et al., 1997; Bout-Roumazeilles et al., 2007; Ehrmann et al., 2007). Consequently, for central-Mediterranean sediments, increased NBEM riverine inputs may be documented by higher illite and chlorite contents, and illite-associated K/Al ratios (e.g. Nijenhuis and de Lange, 2000; Wehausen and Brumsack, 2000; Martinez-Ruiz et al., 2015).

In core CP10/11, illite is thought to be mostly aeolian in origin during non-AHP intervals. By contrast, during the S1a period, the relatively high contents of illite (and associated K/Al) and chlorite, as well as synchronous changes therein are interpreted to reflect enhanced NBEM riverine inputs (Fig. 5b,e,g). This interpretation is supported by the wettest conditions over the NBEM during the S1a interval, as indicated by speleothem $\delta^{18}O$ data and pollen-based precipitation estimates (e.g. Zanchetta et al., 2007; Magny et al., 2013). Moreover, the profiles of K/Al and illite show a close relationship with that of the end member 4-EM3 (modal grain size 3 μm), which represents fine, fluvial particles (Fig. 5b). The narrow grain-size distribution, i.e. good sorting of 4-EM3, suggests a long-range delivery of river-borne material (Fig. 3d). This characterization is similar but more prominent at site ODP964 (Zhao et al., 2016), which is likely to be due to a higher, more proximal riverine contribution enriched in both illite and chlorite (i.e. NBEM) (Fig. 5e,g). By contrast, the NBEM riverine inputs during the AHP, had little effect on the MD04-2797 sediments in the Strait of Sicily (Bout-Roumazeilles et al., 2013), potentially due to the eastward flowing surface waters (Figs. 1 and 5f,h).

A peculiar interval (~6–4 ka) occurs with enhanced 4-EM3 and a low but subsequently increasing K/Al (Fig. 5b). This increase can also be seen in the grain-size records of MD04-2797 (c.f. Bout-Roumazeilles et al., 2013). This may be linked to the onset of enforced circulation because of renewed deepwater formation at the end of sapropel S1 formation (Rohling, 1994; Rohling et al., 2015; Filippidi et al., 2016). The renewed circulation may have caused an intensified flow of surface waters, thereby transporting more shelf-derived material eastward. This material is fine-grained and relatively well-sorted, thus for grain size is assigned to 4-EM3, but its elemental composition, e.g. K/Al, is rather mixed and unrelated to NBEM.

4.2. Characterization of past fluvial discharge from the Libyan-Tunisian margin

We have now distinguished Saharan dust and NBEM riverine inputs for core CP10/11 and attributed these to the first three end members. The 4th end member, 4-EM4, exhibits a close correspondence with the smectite content and Mg/Al (and Ni/Al, Cr/Al) ratios (Fig. 6d–h). This reveals the existence of an important fluvial contribution during the AHP, particularly during the late-AHP, S1b phase. Below, we suggest that this is indicative for paleodrainage discharges from the Libyan-Tunisian margin.

4.2.1. Geochemical and clay-mineral composition

Detrital Mg and K are often associated with chlorite and illite, respectively. This association and the parallel variability of Mg/Al and K/Al in various EMS records have been related to the NBEM riverine inputs enriched in both illite and chlorite (Martinez-Ruiz et al., 2015, and references therein). Such river-borne material is thought to result from weathering of ultramafic rocks (e.g. Wehausen and Brumsack, 2000). In addition, other minerals such as palygorskite and smectite could significantly contribute to the sedimentary Mg content (e.g. Bout-Roumazeilles et al., 2007; Scheuvens et al., 2013; Martinez-Ruiz et al., 2015).

A combination of 1) higher Mg/Al during the AHP and 2) contrasting patterns between Mg/Al and K/Al suggests that the majority of Mg in core CP10/11 was derived from a different riverine source than the NBEM (Figs. 5b and 6e). Above, we discussed that dust and Nile sources can be discounted. Consequently, two potential source areas remain: redeposition from the Strait of Sicily and North-African fluvial discharge. The low detrital Mg/Al ratio

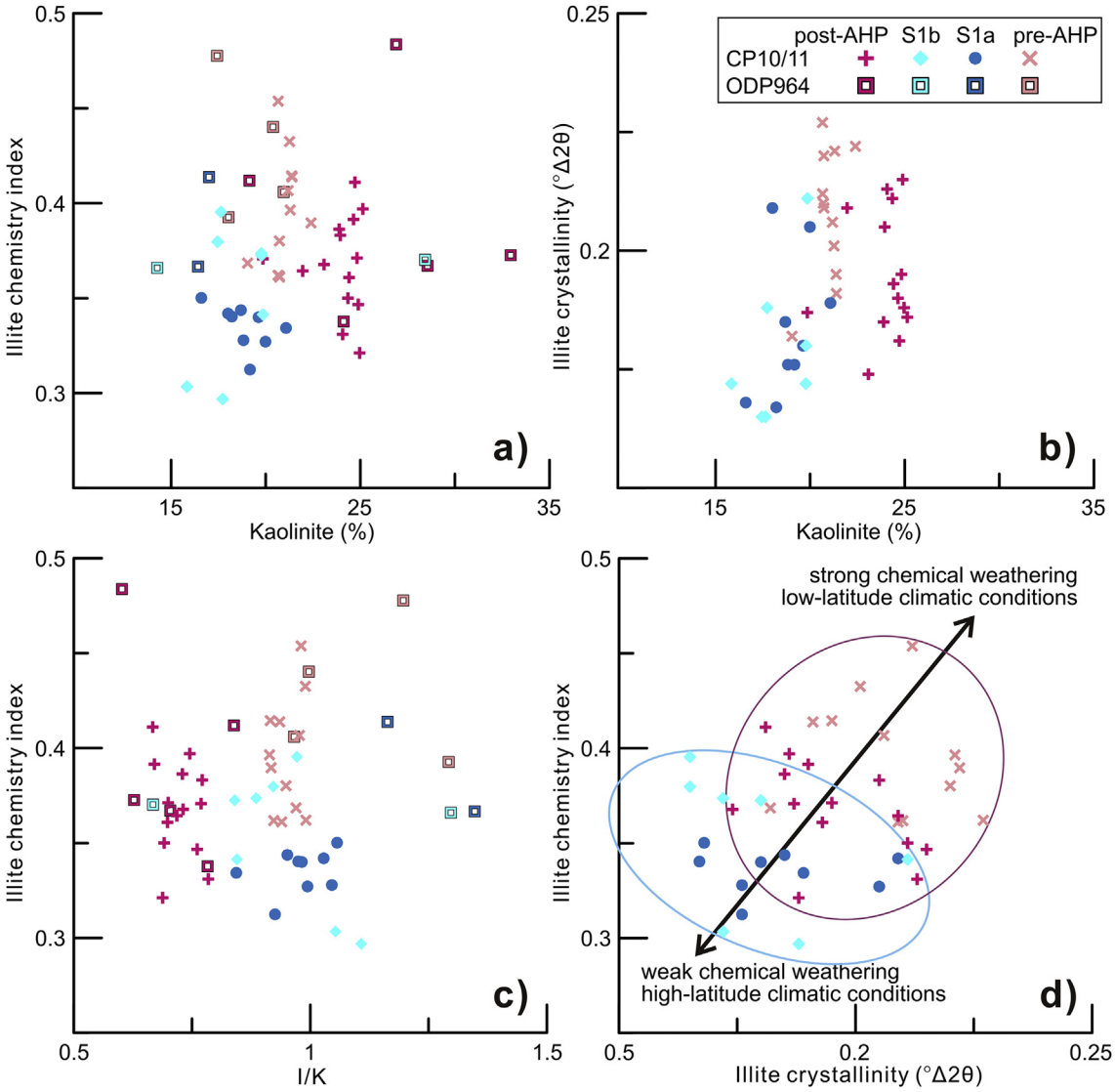

Fig. 7. Plots of illite chemistry index, illite crystallinity, I/K (illite/kaolinite) ratio, and kaolinite content to discriminate different sources of illite for core CP10/11 (also ODP964; Zhao et al., 2016). During non-AHP intervals, the illite is mostly aeolian-origin derived from low latitudes (Saharan dust), whereas during sapropel S1 the illite was mainly delivered by high-latitude (NBEM) riverine inputs. The tephra-related interval (~3.0–1.5 ka) is excluded (see Section 3.1).

observed in sediments from the Strait of Sicily excludes this area as a source (0.11: after Böttcher et al., 2003; 0.110 ± 0.005: G.J. de Lange, unpublished data for Holocene sediments at ODP Site 963).

Instead, the striking similarity between Mg/Al and smectite profiles in core CP10/11 seems to signify that the Mg input is associated with a smectite-rich detrital supply (Fig. 6e,h). Increases in smectite content during sapropel S1 in core CP10/11, and less clearly in ODP964, can also be seen in core MD04-2797 (Bout-Roumazeilles et al., 2013; Zhao et al., 2016) (Fig. 6h,i). Therefore, the correspondence between the Mg/Al and smectite in core CP10/11, and the smectite in cores MD04-2797 and ODP964 is interpreted here to indicate that these multiple-phased changes are controlled by a similar, nearby provenance (Fig. 8e–g). Given the limited supply of Saharan dust during the AHP and the absence of major rivers in this area today, we suggest that the inferred Mg- and smectite-rich detrital supply were delivered via paleodrainage systems from the wider North-African margin. Presently buried under younger aeolian deposits, the paleodrainage systems should have been reactivated during the most-intense humid phase of the AHP (i.e. the S1b). This is in agreement with the deduced composition (low Ti/Al and K/Al) for the detrital supplies from fossil river/wadi systems along the Libyan-Tunisian margin (Wu et al., 2016). In addition, this corresponds with the derived fluvial grain-size end member 4-EM4 (see Section 4.2.2).

In view of the eastward flowing surface waters in the southern central Mediterranean, i.e. across sites MD04-2797 and subsequently CP10/11 and ODP964 (Fig. 1), the coherent changes recorded in these cores may indicate that such paleodrainage-related supplies mainly originated from the west. The most-obvious region is at the Libyan-Tunisian margin, along the Gulf of Gabès. Accordingly, the most-likely route is the Irharhar, which is a large topography-deduced subaerial system interlinked with diverse ephemeral/fossil networks over west Libya and Tunisia/Algeria, with an catchment area of 842,000 km^2 and a length of 1482 km (Vörösmarty et al., 2000; Coulthard et al., 2013) (Fig. 1). Particularly, the Irharhar includes the present-day ephemeral river Medjerda draining Tunisia. Such pathway is supported by the Sr-Nd isotopes gradient of detrital material along a W–E transect in the EMS (Wu et al., 2016), and the extensive geoarchaeological data suggesting more human occupation during the late-AHP in western than in

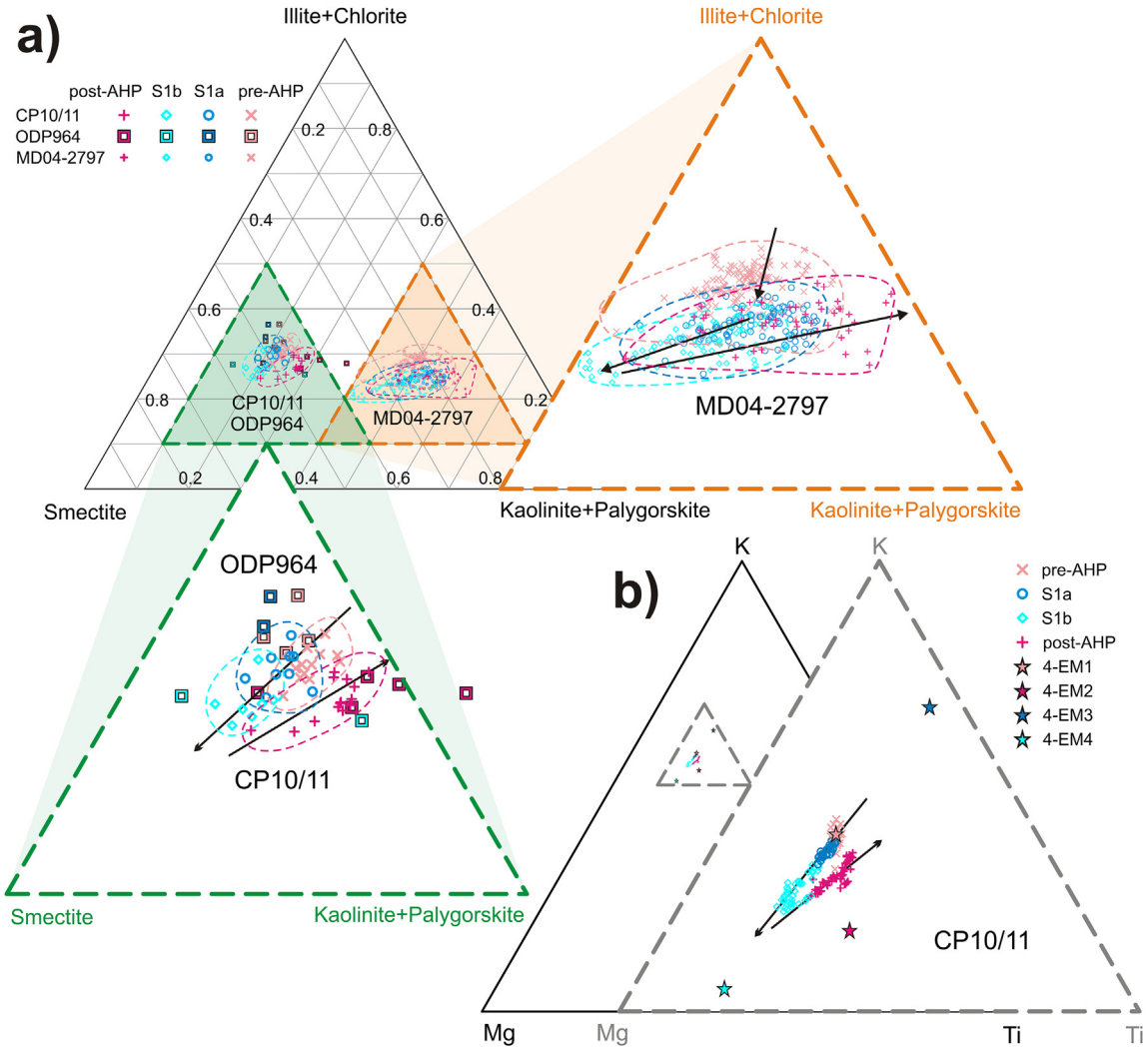

Fig. 8. Ternary diagrams of a) clay minerals and b) detrital elements for central Mediterranean cores. The end members comprise: 1) Saharan dust (kaolinite + palygorskite, Ti), 2) NBEM riverine inputs (illite + chlorite, K), and 3) Libyan-Tunisian fluvial discharge (smectite, Mg). The trends of the clay-mineral data for cores CP10/11, ODP964 (Zhao et al., 2016), and MD04-2797 (Bout-Roumazeilles et al., 2013) are consistent, suggesting enhanced paleodrainage contributions from west Libya and Tunisia/Algeria, during sapropel S1b particularly. For core CP10/11, the detrital-element data not only shows similar trends with those of clay minerals, but also well corresponds with the estimated elemental composition of the grain-size 4-EM end members (Table 2). Note that the elemental pattern is identical whether using Al-normalized or not. The tephra-affected data are excluded (see Section 3.1).

eastern Libya (Manning and Timpson, 2014). Nevertheless, alternative fluvial contributions from eastern Libya towards the Gulf of Sirte, as suggested for sapropel S5, cannot be fully excluded.

The co-varying Mg/Al, Ni/Al, and Cr/Al profiles in core CP10/11 reflect an ultramafic/mafic rock provenance (Fig. 6e–g). There are many ophiolitic and basaltic rocks over the catchment areas of the North-African paleodrainage systems, such as the Hoggar-Acacus Mountains over Algeria and Libya, Tunisian Central Atlas, Tibesti Massif in Libya, and Nafusa Mountains in NE Libya and extending into Tunisia (e.g. Allègre et al., 1981; Kurtz, 1983; Augé et al., 2012; Al-Hafdh and Gafeer, 2015). During the AHP, the reactivated rivers draining catchment areas with occurrences of erodible ultramafic/mafic rock, may have delivered this weathered soil material enriched in Mg, Ni, and Cr to the EMS.

Concurrently, soil deposits over west Libya and Tunisia/Algeria, under recent climatic settings acting as dust source, are characterized by Mg-rich material with a predominance of smectite and palygorskite in the clay-mineral assemblages (Bout-Roumazeilles et al., 2007, 2013). Accordingly, the ephemeral river Medjerda draining western Libya/Tunisia, an important constituent of the Irharhar paleodrainage system (Vörösmarty et al., 2000; Coulthard et al., 2013), is enriched in smectite (up to 50%) in suspended loads (Claude et al., 1977). This river system is thought to have contributed to the high smectite content reported for central-Mediterranean sediments (c.f. Bout-Roumazeilles et al., 2007). During fluvial transport, the initial clay-mineral assemblages may have been modified, as the fragile fibrous palygorskite is mostly destroyed (Chamley, 1989; Bout-Roumazeilles et al., 2007). Such discrepancy of clay-mineral assemblages between the source area and downstream alluvial sediment has also been reported for the Atlas watersheds (Elmouden et al., 2005).

In short, the most likely pathways for the North-African fluvial discharge to the central Mediterranean during the AHP are those through western Libya and Tunisia/Algeria, mainly via the Irharhar paleodrainage system towards the Gulf of Gabès. The provenance of this river-borne material reflects an important component of ultramafic/mafic rock weathering products (i.e. high Mg/Al, Ni/Al, Cr/Al ratios, and smectite content).

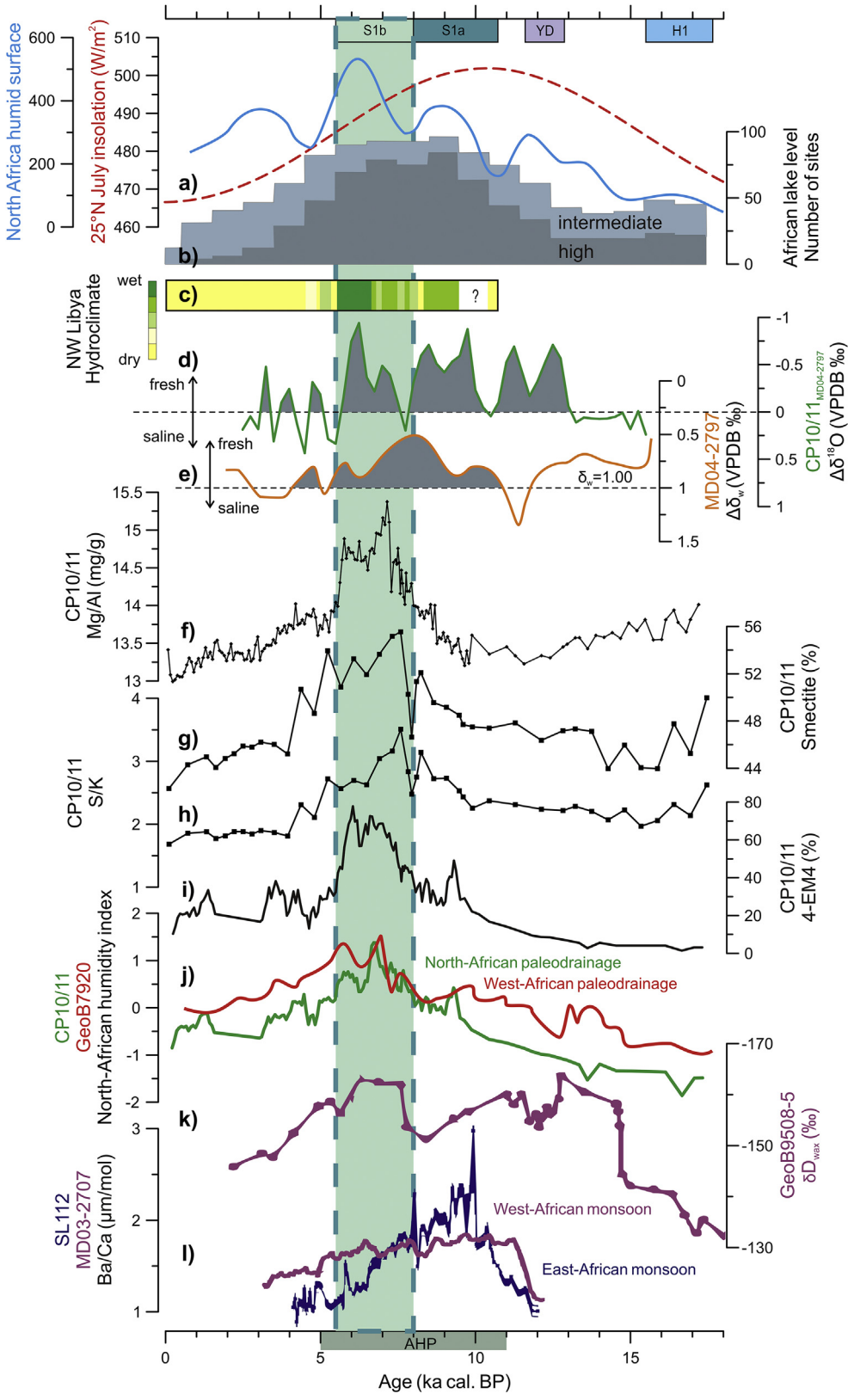

Fig. 9. Hydroclimate proxy records from the central Mediterranean and North Africa display a tight correspondence during late-AHP, S1b interval, inferring a dominant control of North-African humid surface on the paleodrainage delivery, modulated by groundwater level, in response to the insolation-driven West-African monsoon precipitation. a) Mean March insolation at 25°N (Laskar et al., 2004); evolution of estimated (0.85 probability) humid surface over North Africa (10–28°N) (Lézine et al., 2011). b) Lake level status and number of sites in North Africa (after deMenocal and Tierney, 2012). c) Hydroclimate reconstruction of Jefara Plain in NW Libya (Giraudi et al., 2013). d) Planktonic foraminiferal $\Delta\delta^{18}O$ between CP10/11 and MD04-2797. e) Salinity changes recorded by $\Delta\delta_w$ from core MD04-2797 (Essallami et al., 2007). f) Detrital Mg/Al for core CP10/11. g) Smectite in CP10/11. h) S/K (smectite/kaolinite) in CP10/11. i) 4-EM4 proportion, indicative of North-African paleodrainage discharge. j) North-African humidity index derived from grain-size data, expressed as a log-ratio of the North-African fluvial and aeolian end members in CP10/11 and GeoB7920 (Tjallingii et al., 2008; Skonieczny et al., 2015), providing an integrated measure of changes in paleodrainage discharges. k) Hydrogen isotopic composition of leaf waxes (δD_{wax}) in core GeoB9508-5, taken as a direct indicator of changes in West-African monsoon precipitation (Niedermeyer et al., 2010). l) Ba/Ca in planktonic foraminiferal calcite, a proxy for regional riverine runoff and associated monsoon precipitation, retrieved from the Levantine Basin (SL112) and Gulf of Guinea (MD03-2797), respectively (Weldeab et al., 2007, 2014).

4.2.2. Transport processes and depositional environments

Fine-grained fluvial sediments are typically between 4 and 6 μm, and mostly deposited on the continental slope, but can reach the deep basin by nepheloid-layer sedimentation and low-density turbidity (Prins et al., 2000; Stuut et al., 2002). Located at the margin of the Libyan slope, core CP10/11 may have been affected by both processes (Fig. 1a). The hemipelagic end member 4-EM4, having a dominant mode at ~5 μm (Fig. 4d), is inferred as having been settled out of suspension, along with downslope sediment transport.

The downcore profile of 4-EM4 exhibits a close relationship with that of Mg/Al and smectite, suggesting that the 4-EM4 component originates from Libyan-Tunisian paleodrainage systems (Fig. 6d,e,h). Similar grain-size distributions have been proposed as fluvial end members for the West-African margin (e.g. Zühlsdorff et al., 2007; Tjallingii et al., 2008). Besides, the 4-EM4 appears to comprise additional shelf-derived sediments, as seen from a minor peak near 150 μm in the modeled grain-size distribution (Fig. 3d). For the nearby core MD04-2797, a combination of decreases of wind-blown clay minerals (palygorskite and illite) and higher Zr/Al ratios during the S1b interval has been interpreted as an enhanced transport of riverine-sourced sediments to the shelf (Bout-Roumazeilles et al., 2013). Intensified fluvial dynamics over western Libya and Tunisia is likely responsible for those changes. Increased flooding and aggradation of relatively coarse overbank deposits during ~7–6 ka have been reported for the Medjerda alluvial sequences (Zielhofer et al., 2004, 2008). Thus, the increased median grain size of detrital material observed during S1b could be explained by elevated contributions of fluvial component 4-EM4, representing a mixture of fine fluvial particles in particular and of some coarse shelf-derived sediments (Fig. 4a,e).

During the humid climate periods, the reactivated paleodrainage systems could have provoked floods more frequently, because of strong precipitation seasonality (c.f. Zahar et al., 2008). Even during the last few millennia, extreme seasonal flooding is known for the Medjerda, e.g. in the year of 1973, suspension load ~170 g/liter and 10^8 ton of sediment deposited (Jebari et al., 2012). In the headwater region of the Irharhar paleodrainage system, coexisting evidence for freshwater environments and high evaporation rate suggests strong seasonal fluctuations of lake levels during the period of ~6.8–5.7 ka (Cremaschi and Zerboni, 2009; Zerboni et al., 2015). Persistently high winter- and decreased summer-rainfall have also been shown for the southern Mediterranean areas (e.g. Lake Pergusa) during ~7–5 ka (Magny et al., 2013). Also, simulations have shown a most-enhanced monsoon precipitation during S1b resulting from abundant late-summer moisture, which extended the Saharan rainy season into October (Skinner and Poulsen, 2016). These all are in line with the wettest conditions over NW Libya occurring between ~6.8 and 5.5 ka (Giraudi et al., 2013).

The enhanced precipitation and consequent flooding is consistent with the decreased $\delta^{18}O$ ratio of planktonic foraminifera during sapropel S1 observed in cores CP10/11 and MD04-2797 (Fig. 8a). The more negative $\delta^{18}O$ observed for core CP10/11 during the AHP, as indicated by the $\Delta\delta^{18}O$ between CP10/11 and MD04-2797, points to a stronger freshening of surface waters for the former site (Fig. 8b). For core MD04-2797, the negative $\Delta\delta_w$ values (i.e. lower than local seawater $\delta^{18}O$) were calculated using the alkenones-based sea surface temperatures (SST). These $\delta^{18}O$ data suggest a relatively low sea surface salinity for the whole sapropel S1 period (Fig. 8c). Given the proximity and the anticipated eastward flowing surface waters across MD04-2797 towards CP10/11 site (Fig. 1), the observed lower $\delta^{18}O$ for the latter may indicates additional excess freshwater supplies relative to the former. This coincides with the Irharhar runoff discussed above. These observations confirm that the fluvial discharge not only transports the detrital material, but also considerable freshwater.

4.3. Controls on the paleodrainage reactivation and delivery over North Africa

4.3.1. Integrating central-Mediterranean sediment provenance

To summarize, the grain-size data of core CP10/11 can best be described by two aeolian and two fluvial end members, in good agreement with the characterizations based on elemental geochemistry and clay mineralogy. The quantitative estimation of the elemental ratios for the four grain-size end members lends strong supports to our interpretations above, revealing generally high Ti/Al ratios for the aeolian 4-EM1 and 4-EM2, relatively high K/Al for the NBEM riverine inputs (4-EM3), and particularly high Mg/Al for the North-African paleodrainage discharge (4-EM4) (Table 2).

The results from clay minerals and major detrital-elements are presented in adjoining ternary diagrams to further integrate the above-discussed characteristics (Fig. 8). The end members comprise: 1) Saharan dust (high Ti and kaolinite, and palygorskite), 2) NBEM riverine inputs (high K, illite and chlorite), and 3) fluvial discharge from the Libyan-Tunisian margin (high Mg and smectite). Note that the two aeolian end members are considered as one single end member of Saharan dust, as they both have generally high Ti and kaolinite contents, with detectable palygorskite.

Derived from different size fractions, the clay-mineral (Fig. 8a) and elemental (Fig. 8b) data are highly consistent, both displaying a trend towards smectite- and Mg-rich from the pre-AHP to S1b intervals, followed by a trend more towards kaolinite- and Ti-rich signals for the post-AHP. This evolutionary pattern also well corresponds with the estimated elemental composition of the grain-size 4-EM end members (Table 2; Fig. 8b). Together, the remarkable similarity in the data evolution between clay minerals, major detrital-elements, and grain-size distribution strongly corroborates our interpretations above.

After the provenance characterization for central-Mediterranean sediments, critical proxies are extracted to assess the hydroclimate changes over North Africa. Following comparable studies on sediments deposited offshore continental margins (e.g. Stuut et al., 2002; Tjallingii et al., 2008), we use the log-ratio of the North-African fluvial end member (4-EM4) and aeolian end members (4-EM1 + 4-EM2) to indicate relative changes of continental humidity and surface cover in North Africa (Fig. 9j). The use of this proxy is validated by the co-varying S/K ratio for the clay-sized fraction (Fig. 9h), which is interpreted to indicate the relative contribution of North-African fluvial vs. aeolian inputs. Similarly, we use the log-ratio of 4-EM4 and 4-EM3 to evaluate the relative humidity between North Africa and the NBEM regions (Fig. 4g).

4.3.2. Forcing and modulation of North-African paleodrainage discharges

The Libyan-Tunisian fluvial discharge appears to be most pronounced during the sapropel S1b interval, delivering considerable Mg- and smectite-rich detrital material and freshwater to the central Mediterranean Sea (Fig. 9d–j). The strongest discharge can be related to intensified fluvial dynamics and the wettest conditions in western Libya and Tunisia/Algeria (Zielhofer et al., 2004, 2008; Giraudi et al., 2013) (Fig. 9c). Moreover, variability of this North-African fluvial discharge to the central Mediterranean Sea has a tight correspondence with that of a large paleodrainage system towards the West-African margin. Today, the Atlantic continental margin of West Africa between 15 and 25°N is dominated by Saharan arid conditions and receives little fluvial input (Ratmeyer et al., 1999; deMenocal et al., 2000). For this area, several

lines of evidence have shown that during late-Quaternary sapropel times reactivation of the Tamanrasett paleodrainage system contributed to canyon formation and sediment deposition offshore the Mauritania margin (e.g. core GeoB7920; Krastel et al., 2004; Antobreh and Krastel, 2006; Zühlsdorff et al., 2007; Tjallingii et al., 2008; Skonieczny et al., 2015) (Fig. 1; see Section 1). There is a remarkable similarity in the humidity and detrital records between our Mediterranean core CP10/11 and the Atlantic core GeoB7920 (Fig. 9f–j), which seems to indicate a common headwater region, the Hoggar-Acacus Mountains (Fig. 1). Indeed, the central Saharan mountains have been reported to play a crucial role in favoring fluvial supplies to the lowlands over the AHP, which acted as a "water tower" receiving the earlier rainfall/water supply from elevated areas (Hoelzmann et al., 1998; Lézine et al., 2011).

Apart from a common headwater region, such close correspondence between the paleodrainage records from the North- and West-African margins may signify a similar climate forcing and modulation mechanism (Fig. 9). A strengthening of the African monsoon driven by an early Holocene precessional insolation maximum, with associated increases in summer precipitation, is the primary forcing of the AHP (Kutzbach, 1981; Claussen et al., 1999). The co-varying humidity indexes and detrital records for cores CP10/11 and GeoB7920 (Fig. 9f–j) are concurrent with changes in the extension of open-water bodies over North Africa (Fig. 9a), and in contrast to Saharan dust inputs (Fig. 9h). It has been suggested that the North-African surface characteristics exerts a fundamental control on dust emission (Claussen et al., 1999; deMenocal et al., 2000; Egerer et al., 2016). Based on the above-observed correspondence, our results further suggest a similar control on paleodrainage delivery. All of these records show a maximum humidity in the late-AHP, S1b interval (i.e. ~8.0–5.5 ka) (Fig. 9). However, there is a lag of ~3–5 ka with the precessional insolation maxima (Fig. 9a), and records are asynchronous with the precipitation proxy data of the African monsoon (Fig. 9k,l).

This contrast can be best explained by a modulating role of groundwater level, which has been recently highlighted by Lézine et al. (2011) on the basis of a comprehensive examination of >1500 paleohydrological dated records over North Africa. The highest number of lake initiations, associated with enhanced African monsoon precipitation, is recorded in the S1a interval. At that time, however, the geographical extension of open-water bodies was more fragmented and the groundwater was at a relatively low level, resulting in limited paleodrainage-related supplies (Fig. 9a,b). Once the continuously high precipitation has replenished the groundwater to a sufficient level, i.e. after ~8 ka, the fluvial systems including lakes, wetlands, and rivers, were interlinked and fully developed at ~6 ka (Lézine et al., 2011) (Fig. 9a,b). This largest geographical extension of open-water bodies for the late-AHP (i.e. ~8–6 ka) have also been deduced from dust studies, as discussed below (McGee et al., 2013; Cockerton et al., 2014; Egerer et al., 2016). Specifically, lakes and wetlands were widespread up to 30°N and covered ~7.6% of North Africa (Hoelzmann et al., 1998; Jolly et al., 1998). The largest water body was Lake Mega-Chad, which attained an area of 361,000 km^2 and a depth of up to 160 m (c.f. Armitage et al., 2015). There may be even a most-enhanced Saharan precipitation during the late-AHP (Niedermeyer et al., 2010; Skinner and Poulsen, 2016) (Fig. 9k). Therefore, such extensive humid surfaces and persistently wet conditions during the late-AHP, S1b phase should have promoted the paleodrainage-related runoff to the greatest extent (Fig. 9).

Coherently, the largest humid surfaces (Fig. 9a) coincides with the lowest dust input occurred in the late-AHP, S1b interval, as indicated by the S/K ratio (Fig. 9h). This point is also visible in various aeolian parameters (e.g. Ti/Al, kaolinite, 4-EM1, 4-EM2) (Fig. 4b–d and 5a,c). This coincidence reflects the control of North-African humid surfaces on Saharan dust emission. In fact, the most diminished fluxes of Saharan dust (i.e. 2–5 times lower than pre-industrial fluxes) have been systematically reported for the period of ~8–6 ka, in relation to the wettest Saharan landscape (McGee et al., 2013; Cockerton et al., 2014; Egerer et al., 2016). In addition, this inference is in line with the relative humidity between the southern and northern borderlands of the EMS (Fig. 4g). During the AHP and particularly during S1b, climatic conditions were more humid in North Africa (Giraudi et al., 2013), whereas during non-AHP intervals, those in the NBEM were wetter. The former is suggested to be due to a southward shift of the ITCZ during AHP, and the latter is related to sustained high winter precipitation (Magny et al., 2013).

In a broader perspective, we compare our results with precipitation proxy records for the East- and West-African monsoon (Fig. 1b). The record of hydrogen isotopic composition of leaf waxes (δD_{wax}) offshore Senegal (close to GeoB7920), has been interpreted to directly reflect the variability of West-African monsoon precipitation (Niedermeyer et al., 2010) (Fig. 9k). As a reliable proxy for the Nile and the Niger/Sanaga runoffs, the planktonic foraminiferal Ba/Ca records are considered to represent a spatially integrated measure of changes in precipitation of the East- and West-African monsoon, respectively (Weldeab et al., 2007, 2014) (Fig. 9l). It has been suggested that the intensified East-African monsoon during sapropel S1 was largely influenced by Indian Ocean SST variations (Tierney and deMenocal, 2013; Hennekam et al., 2014; Weldeab et al., 2014), while the West-African monsoon precipitation has an Atlantic Ocean moisture source (Schefuβ et al., 2005; Weldeab et al., 2007; Niedermeyer et al., 2010; Shanahan et al., 2015). Consequently, the evolution of East- and West-African monsoon is different (Fig. 9k,l). Placing our results and interpretations in this context, the paleodrainage delivery seems to be primarily controlled by the West-African monsoon, which maintained a high precipitation over the whole AHP (Figs. 1b and 9f–l). This inference is supported by the Sahara/Sahel vulnerability to the Atlantic, West-African monsoon changes in the long-term (Lézine et al., 2011). Furthermore, it is in agreement with various proxy records of West-African monsoon variability, showing persistently enhanced precipitation during the late-AHP, S1b interval (e.g. deMenocal et al., 2000; Schefuβ et al., 2005; Niedermeyer et al., 2010; Shanahan et al., 2015, and references therein).

In summary, the above-discussed correspondences appear to indicate a dominant control of Saharan humid surfaces on the reactivation and delivery of paleodrainage systems over North Africa, which were modulated by groundwater level, in response to insolation-driven West-African monsoon precipitation.

5. Conclusions

On the basis of provenance determination for terrigenous detrital sediments in core CP10/11, we draw the following conclusions for the central Mediterranean during the past 18 ka:

a) During the African Humid period (AHP; ~11–5 ka), largely coinciding with the formation of sapropel S1, riverine deposition to the central Mediterranean dominates, whereas for the preceding and following arid climate periods, the provenance is dust-dominated. Two aeolian and two fluvial end members can be distinguished using end-member modeling of grain-size distributions, elemental and clay mineralogical composition, with their elemental fingerprints quantitatively estimated.
b) The two aeolian end members represent the different supplies of Saharan dust that dominate before and after the AHP. Saharan dust is characterized by generally high Ti and

kaolinite, and detectable palygorskite contents. The different provenance of Saharan dust is related to changes in the meridional position of the ITCZ before and after the AHP, reflecting a large-scale atmospheric reorganization over North Africa.

c) During sapropel S1a (~10.6–8.0 ka), the NBEM (Northern Borderlands of Eastern Mediterranean) riverine inputs rise, as indicated by co-increasing illite and chlorite, and enhanced K contents.

d) During late-AHP, S1b interval (~8.0–5.5 ka), by contrast, riverine inputs appear to be predominantly derived from the North-African, Libyan-Tunisian margin. The inferred fluvial discharge should have transported considerable (Mg- and smectite-rich) detrital materials and freshwater via the paleodrainage networks towards the Gulf of Gabès (mainly via the paleo-river Irharhar). These ancient water courses were reactivated by intensified African monsoon precipitation and were most developed during the late-AHP. This period coincides with the enhanced fluvial dynamics and wettest conditions over western Libya and Tunisia/Algeria. In a wider perspective, the late-AHP, S1b phase is not only synchronous with the lowest supply of Saharan dust and the largest extension of open-water bodies in North Africa, but is also consistent with the West-African monsoon variability. Furthermore, changes in this North-African fluvial discharge correspond with a paleodrainage record offshore the Atlantic, West-African margin, which may indicate a common headwaters' region in the central Saharan mountains, with a similar climate mechanism. Taken together, we propose that the reactivation and delivery of paleodrainage discharges over North Africa were mainly controlled by Saharan humid surfaces, with modulation by groundwater level, in response to the insolation-driven West-African monsoon precipitation.

Acknowledgments

Many thanks are given to Yanli Li who performed the XRD analyses at Tongji University. We acknowledge Arnold van Dijk, Helen de Waard, as well as Dineke van de Meent-Olieman and Ton Zalm for $\delta^{18}O_{ruber}$, ICP-OES, and grain-size analyses at Utrecht University. We also thank Viviane Bout-Roumazeilles and Gert Jan Weltje for kindly providing clay-mineral data of core MD04-2797 and the End-Member Model Algorithm, respectively. We are grateful to crew and scientists on board RV *Pelagia* during CORTADO 2011 cruise for collecting cores CP10BC and CP11PC. Two anonymous reviewers are thanked for their valuable comments and suggestions. The China Scholarship Council – Utrecht University PhD Program is acknowledged for financial support (CSC No. 201206260116).

Appendix A. Supplementary data

Supplementary data related to this article can be found at http://dx.doi.org/10.1016/j.quascirev.2017.03.015.

References

Al-Hafdh, N.M., Gafeer, A.S., 2015. The petrology and geochemistry of Gharyan volcanic province of NW Libya. J. Afr. Earth Sci. 104, 71–102.

Allègre, C.J., Dupré, B., Lambret, B., Richard, P., 1981. The subcontinental versus suboceanic debate, I Lead-neodymium-strontium isotopes in primary alkali basalts from a shield area the Ahaggar volcanic suite. Earth Planet. Sci. Lett. 52, 85–92.

Almogi-Labin, A., Bar-Matthews, M., Shriki, D., Kolosovsky, E., Paterne, M., Schilman, B., Ayalon, A., Aizenshtat, Z., Matthews, A., 2009. Climatic variability during the last similar to 90 ka of the southern and northern Levantine Basin as evident from marine records and speleothems. Quat. Sci. Rev. 28, 2882–2896.

Antobreh, A.A., Krastel, S., 2006. Morphology, seismic characteristics and development of Cap Timiris Canyon, offshore Mauritania: a newly discovered canyon preserved-off a major and climatic region. Mar. Petroleum Geol. 23, 37–59.

Armitage, S.J., Bristow, C.S., Drake, N.A., 2015. West African monsoon dynamics inferred from abrupt fluctuations of Lake Mega-Chad. Proc. Natl. Acad. Sci. U. S. A. 112, 8543–8548.

Augé, T., Joubert, M., Bailly, L., 2012. Typology of mafic-ultramafic complexes in Hoggar, Algeria: implications for PGE, chromite and base-metal sulphide mineralisation. J. Afr. Earth Sci. 63, 32–47.

Barsanti, M., Delbono, I., Schirone, A., Langone, L., Miserocchi, S., Salvi, S., Delfanti, R., 2011. Sediment reworking rates in deep sediments of the Mediterranean Sea. Sci. Total Environ. 409, 2959–2970.

Biscaye, P.E., 1965. Mineralogy and sedimentation of recent deep-sea clay in Atlantic Ocean and adjacent seas and oceans. Geol. Soc. Am. Bull. 76, 803–832.

Böttcher, M.E., Rinna, J., Warning, B., Wehausen, R., Howell, M.W., Schnetger, B., Stein, R., Brumsack, H.J., Rullkotter, J., 2003. Geochemistry of sediments from the connection between the western and the eastern Mediterranean Sea (Strait of Sicily, ODP site 963). Palaeogeogr. Palaeoclimatol. Palaeoecol. 190, 165–194.

Bout-Roumazeilles, V., Nebout, N.C., Peyron, O., Cortijo, E., Landais, A., Masson-Delmotte, V., 2007. Connection between South Mediterranean climate and North African atmospheric circulation during the last 50,000 yr BP North Atlantic cold events. Quat. Sci. Rev. 26, 3197–3215.

Bout-Roumazeilles, V., Combourieu-Nebout, N., Desprat, S., Siani, G., Turon, J.L., Essallami, L., 2013. Tracking atmospheric and riverine terrigenous supplies variability during the last glacial and the Holocene in central Mediterranean. Clim. Past 9, 1065–1087.

Caquineau, S., Gaudichet, A., Gomes, L., Magonthier, M.C., Chatenet, B., 1998. Saharan dust: clay ratio as a relevant tracer to assess the origin of soil-derived aerosols. Geophys. Res. Lett. 25, 983–986. http://dx.doi.org/10.1029/2000JD000247.

Chamley, H., 1989. Clay Sedimentology. Springer, Berlin, 623 pp.

Claude, J., Francillon, G., Loyer, J.Y., 1977. Les alluvions déposées par l'Oued Medjerda lors de la crue exceptionnelle de mars 1973. Cah. l'Orstom, sér. Hydrol. 14, 37–109.

Claussen, M., Kubatzki, C., Brovkin, V., Ganopolski, A., Hoelzmann, P., Pachur, H.J., 1999. Simulation of an abrupt change in Saharan vegetation in the mid-Holocene. Geophys. Res. Lett. 26, 2037–2040.

Clemens, S.C., 1998. Dust response to seasonal atmospheric forcing: proxy evaluation and calibration. Paleoceanography 13, 471–490.

Cockerton, H.E., Holmes, J.A., Street-Perrott, F.A., Ficken, K.J., 2014. Holocene dust records from the West African Sahel and their implications for changes in climate and land surface conditions. J. Geophys. Res. Atmos. 119, 8684–8694.

Coulthard, T.J., Ramirez, J.A., Barton, N., Rogerson, M., Brücher, T., 2013. Were rivers flowing across the Sahara during the last Interglacial? Implications for human migration through Africa. PloS ONE 8, e74834. http://dx.doi.org/10.1371/journal.pone.0074834.

Cremaschi, M., Zerboni, A., 2009. Early to Middle Holocene landscape exploitation in a drying environment: two case studies compared from the central Sahara (SW Fezzan, Libya). Comptes Rendus Geosci. 341, 689–702.

De Lange, G.J., Thomson, J., Reitz, A., Slomp, C.P., Principato, M.S., Erba, E., Corselli, C., 2008. Synchronous basin-wide formation and redox-controlled preservation of a Mediterranean sapropel. Nat. Geosci. 1, 606–610.

deMenocal, P., Ortiz, J., Guilderson, T., Adkins, J., Sarnthein, M., Baker, L., Yarusinsky, M., 2000. Abrupt onset and termination of the African Humid Period: rapid climate responses to gradual insolation forcing. Quat. Sci. Rev. 19, 347–361.

deMenocal, P., Tierney, J., 2012. Green Sahara: African humid periods paces by Earth's orbital changes. Nat. Educ. Knowl. 3, 10.

Drake, N.A., Blench, R.M., Armitage, S.J., Bristow, C.S., White, K.H., 2011. Ancient watercourses and biogeography of the Sahara explain the peopling of the desert. Proc. Natl. Acad. Sci. U. S. A. 108, 458–462.

Egerer, S., Claussen, M., Reick, C., Stanelle, T., 2016. The link between marine sediment records and changes in Holocene Saharan landscape: simulating the dust cycle. Clim. Past 12, 1009–1027.

Ehrmann, W., Schmiedl, G., Hamann, Y., Kuhnt, T., 2007. Distribution of clay minerals in surface sediments of the Aegean Sea: a compilation. Int. J. Earth Sci. 96, 769–780.

Elmouden, A., Bouchaou, L., Snoussi, M., 2005. Constraints on alluvial clay mineral assemblages in semiarid regions. The Souss Wadi Basin (Morocco, Northwestern Africa). Geol. Acta 3, 3–13.

Emeis, K.C., Schulz, H., Struck, U., Rossignol-Strick, M., Erlenkeuser, H., Howell, M.W., Kroon, D., Mackensen, A., Ishizuka, S., Oba, T., Sakamoto, T., Koizumi, I., 2003. Eastern Mediterranean surface water temperatures and $\delta^{18}O$ composition during deposition of sapropels in the late Quaternary. Paleoceanography 18, 1005. http://dx.doi.org/10.1029/2000PA000617.

Essallami, L., Sicre, M.A., Kallel, N., Labeyrie, L., Siani, G., 2007. Hydrological changes in the Mediterranean Sea over the last 30,000 years. Geochem. Geophys. Geosystems 8, Q07002. http://dx.doi.org/10.1029/2007GC001587.

Filippidi, A., Triantaphyllou, M.V., De Lange, G.J., 2016. Eastern-Mediterranean ventilation variability during sapropel S1 formation, evaluated at two sites influenced by deep-water formation from Adriatic and Aegean Seas. Quat. Sci. Rev. 144, 95–106.

Freydier, R., Michard, A., de Lange, G.J., Thomson, J., 2001. Nd isotopic compositions of Eastern Mediterranean sediments: tracers of the Nile influence during

sapropel S1 formation? Mar. Geol. 177, 45–62.
Giraudi, C., Mercuri, A.M., Esu, D., 2013. Holocene palaeoclimate in the northern Sahara margin (Jefara Plain, northwestern Libya). Holocene 23, 339–352.
Grimm, R., Maier-Reimer, E., Mikolajewicz, U., Schmiedl, G., Muller-Navarra, K., Adloff, F., Grant, K.M., Ziegler, M., Lourens, L.J., Emeis, K.C., 2015. Late glacial initiation of Holocene eastern Mediterranean sapropel formation. Nat. Commun. 6, 7099. http://dx.doi.org/10.1038/ncomms8099.
Guerzoni, S., Molinaroli, E., Chester, R., 1997. Saharan dust inputs to the western Mediterranean Sea: depositional patterns, geochemistry and sedimentological implications. Deep-Sea Res. Part II Topical Stud. Oceanogr. 44, 631–654.
Hamann, Y., Ehrmann, W., Schmiedl, G., Kruger, S., Stuut, J.B., Kuhnt, T., 2008. Sedimentation processes in the Eastern Mediterranean Sea during the Late Glacial and Holocene revealed by end-member odeling of the terrigenous fraction in marine sediments. Mar. Geol. 248, 97–114.
Hamann, Y., Ehrmann, W., Schmiedl, G., Kuhnt, T., 2009. Modern and late Quaternary clay mineral distribution in the area of the SE Mediterranean Sea. Quat. Res. 71, 453–464.
Hennekam, R., Jilbert, T., Schnetger, B., de Lange, G.J., 2014. Solar forcing of Nile discharge and sapropel S1 formation in the early to middle Holocene eastern Mediterranean. Paleoceanography 29, 343–356.
Hennekam, R., Donders, T., Zwiep, K., de Lange, G., 2015. Integral view of Holocene precipitation and vegetation changes in the Nile catchment area as inferred from its delta sediments. Quat. Sci. Rev. 130, 189–199.
Hoelzmann, P., Jolly, D., Harrison, S.P., Laarif, F., Bonnefille, R., Pachur, H.J., 1998. Mid-Holocene land-surface conditions in northern Africa and the Arabian Peninsula: a data set for the analysis of biogeophysical feedbacks in the climate system. Glob. Biogeochem. Cycles 12, 35–51.
Jebari, S., Berndtsson, R., Lebdi, F., Bahri, A., 2012. Historical aspects of soil erosion in the Mejerda catchment, Tunisia. Hydrol. Sci. J. 57, 901–912.
Jolly, D., Harrison, S.P., Damnati, B., Bonnefille, R., 1998. Simulated climate and biomes of Africa during the late quaternary: comparison with pollen and lake status data. Quat. Sci. Rev. 17, 629–657.
Kallel, N., Paterne, M., Duplessy, J.C., VergnaudGrazzini, C., Pujol, C., Labeyrie, L., Arnold, M., Fontugne, M., Pierre, C., 1997. Enhanced rainfall in the Mediterranean region during the last sapropel event. Oceanol. Acta 20, 697–712.
Krastel, S., Hanebuth, T.J.J., Antobreh, A.A., Henrich, R., Holz, C., Kölling, M., Schulz, H.D., Wien, K., Wynn, R.B., 2004. Cap Timiris Canyon: a newly discovered channel-system off Mauritania. EOS Trans. Am. Geophys. Union 85, 417–432.
Krom, M.D., Cliff, R.A., Eijsink, L.M., Herut, B., Chester, R., 1999a. The characterisation of Saharan dusts and Nile particulate matter in surface sediments from the Levantine basin using Sr isotopes. Mar. Geol. 155, 319–330.
Krom, M.D., Michard, A., Cliff, R.A., Strohle, K., 1999b. Sources of sediment to the Ionian Sea and western Levantine Basin of the Eastern Mediterranean during S-1 sapropel times. Mar. Geol. 160, 45–61.
Kuper, R., Kropelin, S., 2006. Climate-controlled holocene occupation in the Sahara: Motor of Africa's evolution. Science 313, 803–807.
Kurtz, J., 1983. Geochemistry of Early Mesozoic basalts from Tunisia. J. Afr. Earth Sci. 1, 113–125.
Kutzbach, J.E., 1981. Monsoon climate of the early holocene - climate experiment with the earths orbital parameters for 9000 years ago. Science 214, 59–61.
Larrasoaña, J.C., Roberts, A.P., Rohling, E.J., Winklhofer, M., Wehausen, R., 2003. Three million years of monsoon variability over the northern Sahara. Clim. Dyn. 21, 689–698.
Larrasoaña, J.C., Roberts, A.P., Rohling, E.J., 2013. Dynamics of green Sahara periods and their role in hominin evolution. Plos One 8, e76514. http://dx.doi.org/10.1371/journal.pone.0076514.
Laskar, J., Robutel, P., Joutel, F., Gastineau, M., Correia, A.C.M., Levrard, B., 2004. A long-term numerical solution for the insolation quantities of the Earth. Astronomy Astrophys. 428, 261–285.
Lézine, A.M., Hely, C., Grenier, C., Braconnot, P., Krinner, G., 2011. Sahara and Sahel vulnerability to climate changes, lessons from Holocene hydrological data. Quat. Sci. Rev. 30, 3001–3012.
Liu, Z.F., Colin, C., Trentesaux, A., Blamart, D., Bassinot, F., Siani, G., Sicre, M.A., 2004. Erosional history of the eastern Tibetan Plateau since 190 kyr ago: clay mineralogical and geochemical investigations from the southwestern South China Sea. Mar. Geol. 209, 1–18.
Lourens, L.J., Wehausen, R., Brumsack, H.J., 2001. Geological constraints on tidal dissipation and dynamical ellipticity of the Earth over the past three million years. Nature 409, 1029–1033.
Magny, M., Combourieu-Nebout, N., de Beaulieu, J.L., Bout-Roumazeilles, V., Colombaroli, D., Desprat, S., Francke, A., Joannin, S., Ortu, E., Peyron, O., Revel, M., Sadori, L., Siani, G., Sicre, M.A., Samartin, S., Simonneau, A., Tinner, W., Vanniere, B., Wagner, B., Zanchetta, G., Anselmetti, F., Brugiapaglia, E., Chapron, E., Debret, M., Desmet, M., Didier, J., Essallami, L., Galop, D., Gilli, A., Haas, J.N., Kallel, N., Millet, L., Stock, A., Turon, J.L., Wirth, S., 2013. North-south palaeohydrological contrasts in the central Mediterranean during the Holocene: tentative synthesis and working hypotheses. Clim. Past 9, 2043–2071.
Manning, K., Timpson, A., 2014. The demographic response to Holocene climate change in the Sahara. Quat. Sci. Rev. 101, 28–35.
Martinez-Ruiz, F., Kastner, M., Gallego-Torres, D., Rodrigo-Gamiz, M., Nieto-Moreno, V., Ortega-Huertas, M., 2015. Paleoclimate and paleoceanography over the past 20,000 yr in the Mediterranean Sea Basins as indicated by sediment elemental proxies. Quat. Sci. Rev. 107, 25–46.
McGee, D., deMenocal, P.B., Winckler, G., Stuut, J.B.W., Bradtmiller, L.I., 2013. The magnitude, timing and abruptness of changes in North African dust deposition over the last 20,000 yr. Earth Planet. Sci. Lett. 371, 163–176.
Niedermeyer, E.M., Schefuß, E., Sessions, A.L., Mulitza, S., Mollenhauer, G., Schulz, M., Wefer, G., 2010. Orbital- and millennial-scale changes in the hydrologic cycle and vegetation in the western African Sahel: insights from individual plant wax δD and $\delta^{13}C$. Quat. Sci. Rev. 29, 2996–3005.
Nijenhuis, I.A., de Lange, G.J., 2000. Geochemical constraints on Pliocene sapropel formation in the eastern Mediterranean. Mar. Geol. 163, 41–63.
Osborne, A.H., Vance, D., Rohling, E.J., Barton, N., Rogerson, M., Fello, N., 2008. A humid corridor across the Sahara for the migration of early modern humans out of Africa 120,000 years ago. Proc. Natl. Acad. Sci. U. S. A. 105, 16444–16447.
Osborne, A.H., Marino, G., Vance, D., Rohling, E.J., 2010. Eastern Mediterranean surface water Nd during Eemian sapropel S5: monitoring northerly (mid-latitude) versus southerly (sub-tropical) freshwater contributions. Quat. Sci. Rev. 29, 2473–2483.
Paillou, P., Schuster, M., Tooth, S., Farr, T., Rosenqvist, A., Lopez, S., Malezieux, J.M., 2009. Mapping of a major paleodrainage system in eastern Libya using orbital imaging radar: the Kufrah River. Earth Planet. Sci. Lett. 277, 327–333.
Paillou, P., Tooth, S., Lopez, S., 2012. The Kufrah paleodrainage system in Libya: a past connection to the Mediterranean Sea? Comptes Rendus Geosci. 344, 406–414.
Petschick, R., Kuhn, G., Gingele, F., 1996. Clay mineral distribution in surface sediments of the South Atlantic: Sources, transport, and relation to oceanography. Mar. Geol. 130, 203–229.
Petschick, R., 2000. MacDiff 4.2.2.
Pinardi, N., Masetti, E., 2000. Variability of the large scale general circulation of the Mediterranean Sea from observations and modelling: a review. Palaeogeogr. Palaeoclimatol. Palaeoecol. 158, 153–174.
Prins, M., Postma, G., Weltje, G.J., 2000. Controls on terrigenous sediment supply to the Arabian Sea during the late Quaternary: the Makran continental slope. Mar. Geol. 169, 351–371.
Ratmeyer, V., Fischer, G., Wefer, G., 1999. Lithogenic particle fluxes and grain size distributions in the deep ocean off northwest Africa: implications for seasonal changes of aeolian dust input and downward transport. Deep-Sea Res. Part I Oceanogr. Res. Pap. 46, 1289–1337.
Reimer, P.J., Bard, E., Bayliss, A., Beck, J.W., Blackwell, P.G., Ramsey, C.B., Buck, C.E., Cheng, H., Edwards, R.L., Friedrich, M., Grootes, P.M., Guilderson, T.P., Haflidason, H., Hajdas, I., Hatte, C., Heaton, T.J., Hoffmann, D.L., Hogg, A.G., Hughen, K.A., Kaiser, K.F., Kromer, B., Manning, S.W., Niu, M., Reimer, R.W., Richards, D.A., Scott, E.M., Southon, J.R., Staff, R.A., Turney, C.S.M., van der Plicht, J., 2013. Intcal13 and Marine13 radiocarbon age calibration curves, 0–50,000 years cal BP. Radiocarbon 55, 1869–1887.
Reitz, A., Thomson, J., de Lange, G.J., Hensen, C., 2006. Source and development of large manganese enrichments above eastern Mediterranean sapropel S1. Paleoceanography 21, PA3007. http://dx.doi.org/10.1029/2005PA001169.
Revel, M., Ducassou, E., Grousset, F.E., Bernasconi, S.M., Migeon, S., Revillon, S., Mascle, J., Murat, A., Zaragosi, S., Bosch, D., 2010. 100,000 Years of African monsoon variability recorded in sediments of the Nile margin. Quat. Sci. Rev. 29, 1342–1362.
Rohling, E.J., 1994. Review and new aspects concerning the formation of Eastern Mediterranean sapropels. Mar. Geol. 122, 1–28.
Rohling, E.J., Cane, T.R., Cooke, S., Sprovieri, M., Bouloubassi, I., Emeis, K.C., Schiebel, R., Kroon, D., Jorissen, F.J., Lorre, A., Kemp, A.E.S., 2002. African monsoon variability during the previous interglacial maximum. Earth Planet. Sci. Lett. 202, 61–75.
Rohling, E.J., Sprovieri, M., Cane, T., Casford, J.S.L., Cooke, S., Bouloubassi, I., Emeis, K.C., Schiebel, R., Rogerson, M., Hayes, A., Jorissen, F.J., Kroon, D., 2004. Reconstructing past planktic foraminiferal habitats using stable isotope data: a case history for Mediterranean sapropel S5. Mar. Micropaleontol. 50, 89–123.
Rohling, E.J., Pälike, H., 2005. Centennial-scale climate cooling with a sudden cold event around 8,200 years ago. Nature 434, 975–979.
Rohling, E.J., Marino, G., Grant, K.M., 2015. Mediterranean climate and oceanography, and the periodic development of anoxic events (sapropels). Earth Sci. Rev. 143, 62–97.
Rossignol-Strick, M., Nesteroff, W., Olive, P., Vergnaud-Grazzini, C., 1982. After the deluge: Mediterranean stagnation and sapropel formation. Nature 295, 105–110.
Rutten, A., de Lange, G.J., Ziveri, P., Thomson, J., van Santvoort, P.J.M., Colley, S., Corselli, C., 2000. Recent terrestrial and carbonate fluxes in the pelagic eastern Mediterranean: a comparison between sediment trap and surface sediment. Palaeogeogr. Palaeoclimatol. Palaeoecol. 158, 197–213.
Sarnthein, M., Tetzlaff, G., Koopmann, B., Wolter, K., Pflaumann, U., 1981. Glacial and interglacial wind regimes over the eastern subtropical Atlantic and North-West Africa. Nature 293, 193–196.
Schefuß, E., Schouten, S., Schneider, R.R., 2005. Climatic controls on central African hydrology during the past 20,000 years. Nature 437, 1003–1006.
Scheuvens, D., Schutz, L., Kandler, K., Ebert, M., Weinbruch, S., 2013. Bulk composition of northern African dust and its source sediments–A compilation. Earth Sci. Rev. 116, 170–194.
Schroeder, A., Wiesner, M.G., Liu, Z.F., 2015. Fluxes of clay minerals in the South China Sea. Earth Planet. Sci. Lett. 430, 30–42.
Scrivner, A.E., Vance, D., Rohling, E.J., 2004. New neodymium isotope data quantify Nile involvement in Mediterranean anoxic episodes. Geology 32, 565–568.
Shanahan, T.M., McKay, N.P., Hughen, K.A., Overpeck, J.T., Otto-Bliesner, B., Heil, C.W., King, J., Scholz, C.A., Peck, J., 2015. The time-transgressive

termination of the African humid period. Nat. Geosci. 8, 140–144.
Siani, G., Paterne, M., Arnold, M., Bard, E., Metivier, B., Tisnerat, N., Bassinot, F., 2000. Radiocarbon reservoir ages in the Mediterranean Sea and black Sea. Radiocarbon 42, 271–280.
Sirocko, F., Sarnthein, M., Lange, H., Erlenkeuser, H., 1991. Atmospheric summer circulation and coastal upwelling in the Arabian Sea during the holocene and the last Glaciation. Quat. Res. 36, 72–93.
Skinner, C.B., Poulsen, C.J., 2016. The role of fall season tropical plumes in enhancing Saharan rainfall during the African Humid Period. Geophys. Res. Lett. 43, 349–358.
Skonieczny, C., Bory, A., Bout-Roumazeilles, V., Abouchami, W., Galer, S.J.G., Crosta, X., Diallo, A., Ndiaye, T., 2013. A three-year time series of mineral dust deposits on the West African margin: sedimentological and geochemical signatures and implications for interpretation of marine paleo-dust records. Earth Planet. Sci. Lett. 364, 145–156.
Skonieczny, C., Paillou, P., Bory, A., Bayon, G., Biscara, L., Crosta, X., Eynaud, F., Malaize, B., Revel, M., Aleman, N., Barusseau, J.P., Vernet, R., Lopez, S., Grousset, F., 2015. African humid periods triggered the reactivation of a large river system in Western Sahara. Nat. Commun. 6, 8751. http://dx.doi.org/10.1038/ncomms9751.
Stuiver, M., Reimer, P.J., 1993. Extended ^{14}C data-base and revised Calib 3.0 ^{14}C age calibration program. Radiocarbon 35, 215–230.
Stumpf, R., Frank, M., Schonfeld, J., Haley, B.A., 2011. Climatically driven changes in sediment supply on the SW Iberian shelf since the Last Glacial Maximum. Earth Planet. Sci. Lett. 312, 80–90.
Stuut, J.-B.W., Prins, M.A., Schneider, R.R., Weltje, G.J., Jansen, J.H.F., Postma, G., 2002. A 300-kyr record of aridity and wind strength in southwestern Africa: inferences from grain-size distributions of sediments on Walvis Ridge, SE Atlantic. Mar. Geol. 180, 221–233.
Stuut, J.-B.W., Zabel, M., Ratmeyer, V., Helmke, P., Schefuß, E., Lavik, G., Schneider, R.R., 2005. Provenance of present-day eolian dust collected off NW Africa. J. Geophys. Res. Atmos. 110, D04202. http://dx.doi.org/10.1029/2004JD005161.
Tierney, J.E., deMenocal, P.B., 2013. Abrupt shifts in horn of Africa hydroclimate since the last glacial maximum. Science 342, 843–846.
Timmermann, A., Friedrich, T., 2016. Late Pleistocene climate drivers of early human migration. Nature 538, 92–95.
Tjallingii, R., Claussen, M., Stuut, J.B.W., Fohlmeister, J., Jahn, A., Bickert, T., Lamy, F., Rohl, U., 2008. Coherent high- and low-latitude control of the northwest African hydrological balance. Nat. Geosci. 1, 670–675.
Tuenter, E., Weber, S.L., Hilgen, F.J., Lourens, L.J., 2003. The response of the African summer monsoon to remote and local forcing due to precession and obliquity. Glob. Planet. Change 36, 219–235.
Van Santvoort, P.J.M., de Lange, G.J., Thomson, J., Cussen, H., Wilson, T.R.S., Krom, M.D., Ströhle, K., 1996. Active post-depositional oxidation of the most recent sapropel (S1) in sediments of the eastern Mediterranean Sea. Geochim. Cosmochim. Acta 60, 4007–4024.
Venkatarathnam, K., Ryan, W.B.F., 1971. Dispersal patterns of clay minerals in sediments of the eastern Mediterranean Sea. Mar. Geol. 11, 261–282.
Vörösmarty, C.J., Fekete, B.M., Meybeck, M., Lammers, R.B., 2000. Global system of rivers: its role in organizing continental land mass and defining land-to-ocean linkages. Glob. Biogeochem. Cycles 14, 599–621.
Wehausen, R., Brumsack, H.J., 2000. Chemical cycles in Pliocene sapropel-bearing and sapropel-barren eastern Mediterranean sediments. Palaeogeogr. Palaeoclimatol. Palaeoecol. 158, 325–352.
Weldeab, S., Emeis, K.C., Hemleben, C., Siebel, W., 2002a. Provenance of lithogenic surface sediments and pathways of riverine suspended matter in the Eastern Mediterranean Sea: evidence from ^{143}Nd/^{144Nd} and ^{87}Sr/^{86}Sr ratios. Chem. Geol. 186, 139–149.
Weldeab, S., Emeis, K.C., Hemleben, C., Vennemann, T.W., Schulz, H., 2002b. Sr and Nd isotope composition of Late Pleistocene sapropels and nonsapropelic sediments from the Eastern Mediterranean Sea: implications for detrital influx and climatic conditions in the source areas. Geochim. Cosmochim. Acta 66, 3585–3598.
Weldeab, S., Lea, D.W., Schneider, R.R., Andersen, N., 2007. 155,000 years of West African monsoon and ocean thermal evolution. Science 316, 1303–1307.
Weldeab, S., Menke, V., Schmiedl, G., 2014. The pace of East African monsoon evolution during the Holocene. Geophys. Res. Lett. 41, 1724–1731.
Weltje, G.J., 1997. End-member modeling of compositional data: Numerical-statistical algorithms for solving the explicit mixing problem. Math. Geol. 29, 503–549.
Wu, J., Liu, Z., Zhou, C., 2012. Late quaternary glacial cycle and precessional period of clay mineral assemblages in the western pacific warm pool. Chin. Sci. Bull. 57, 3748–3760.
Wu, J., Liu, Z.F., Zhou, C., 2013. Provenance and supply of Fe-enriched terrigenous sediments in the western equatorial Pacific and their relation to precipitation variations during the late Quaternary. Glob. Planet. Change 108, 56–71.
Wu, J., Böning, P., Pahnke, K., Tachikawa, K., De Lange, G.J., 2016. Unraveling North-African riverine and eolian contributions to central Mediterranean sediments during Holocene sapropel S1 formation. Quat. Sci. Rev. 152, 31–48.
Zahar, Y., Ghorbel, A., Albergel, J., 2008. Impacts of large dams on downstream flow conditions of rivers: aggradation and reduction of the Medjerda channel capacity downstream of the Sidi Salem dam (Tunisia). J. Hydrol. 351, 318–330.
Zanchetta, G., Drysdale, R.N., Hellstrom, J.C., Fallick, A.E., Isola, I., Gagan, M.K., Pareschi, M.T., 2007. Enhanced rainfall in the Western Mediterranean during deposition of sapropel S1: stalagmite evidence from Corchia cave (Central Italy). Quat. Sci. Rev. 26, 279–286.
Zerboni, A., Perego, A., Cremaschi, M., 2015. Geomorphological map of the Tadrart Acacus Massif and the Erg Uan Kasa (Libyan Central Sahara). J. Maps 11, 772–787.
Zhao, Y.L., Colin, C., Liu, Z.F., Paterne, M., Siani, G., Xie, X., 2012. Reconstructing precipitation changes in northeastern Africa during the Quaternary by clay mineralogical and geochemical investigations of Nile deep-sea fan sediments. Quat. Sci. Rev. 57, 58–70.
Zhao, Y.L., Colin, C., Liu, Z.F., Bonneau, L., Siani, G., 2016. Climate forcing of terrigenous sediment input to the central Mediterranean Sea since the early Pleistocene. Palaeogeogr. Palaeoclimatol. Palaeoecol. 442, 23–35.
Zielhofer, C., Faust, D., Escudero, R.B., del Olmo, F.D., Kadereit, A., Moldenhauer, K.M., Porras, A., 2004. Centennial-scale late-Pleistocene to mid-Holocene synthetic profile of the Medjerda Valley, northern Tunisia. Holocene 14, 851–861.
Zielhofer, C., Faust, D., Linstadter, J., 2008. Late Pleistocene and Holocene alluvial archives in the Southwestern Mediterranean: changes in fluvial dynamics and past human response. Quat. Int. 181, 39–54.
Zühlsdorff, C., Wien, K., Stuut, J.B.W., Henrich, R., 2007. Late Quaternary sedimentation within a submarine channel-levee system offshore Cap Timiris, Mauritania. Mar. Geol. 240, 217–234.